



HAL
open science

Distribution of indium, germanium, gallium and other minor and trace elements in polymetallic ores from a porphyry system: The Morococha district, Peru

Diego Benites, Lisard Torr , Jean Vallance, Oscar Laurent, Pablo Valverde, Kalin Kouzmanov, Cyril Chelle-Michou, Llu s Fontbot 

► To cite this version:

Diego Benites, Lisard Torr , Jean Vallance, Oscar Laurent, Pablo Valverde, et al.. Distribution of indium, germanium, gallium and other minor and trace elements in polymetallic ores from a porphyry system: The Morococha district, Peru. *Ore Geology Reviews*, 2021, 136, pp.104236. 10.1016/j.oregeorev.2021.104236 . hal-03436621

HAL Id: hal-03436621

<https://hal.science/hal-03436621>

Submitted on 21 Nov 2022

HAL is a multi-disciplinary open access archive for the deposit and dissemination of scientific research documents, whether they are published or not. The documents may come from teaching and research institutions in France or abroad, or from public or private research centers.

L'archive ouverte pluridisciplinaire **HAL**, est destin e au d p t et   la diffusion de documents scientifiques de niveau recherche, publi s ou non,  manant des  tablissements d'enseignement et de recherche fran ais ou  trangers, des laboratoires publics ou priv s.

Distribution of indium, germanium, gallium and other minor and trace elements in polymetallic ores from a porphyry system: The Morococha district, Peru

Diego Benites^a, Lisard Torró^a, Jean Vallance^a, Oscar Laurent^b, Pablo E. Valverde^a, Kalin Kouzmanov^c, Cyril Chelle-Michou^a, Luis Fontboté^c

^aGeological Engineering Program, Faculty of Sciences and Engineering, Pontifical Catholic University of Peru (PUCP), Av. Universitaria 1801, San Miguel, Lima 15088, Peru

^bDepartment of Earth Sciences, ETH Zürich, CH-8092 Zürich, Switzerland

^cDepartment of Earth Sciences, University of Geneva, CH-1205 Geneva, Switzerland

Abstract

We report indium, germanium, gallium, and other minor and trace elements contents in sphalerite, chalcopyrite, galena, and tetrahedrite-tennantite occurring in skarn and skarn-free (“Cordilleran”) polymetallic mantos and vein ore bodies in the Miocene porphyry-related Morococha District, Central Peru. Among the investigated minerals, LA-ICP-MS measurements indicate that In and Ga concentrate mostly in sphalerite (Inter-Quartile Range [IQR] 217–2.7 ppm and up to 4608 ppm In; IQR 61–2.0 ppm and up to 2137 ppm Ga) and chalcopyrite (IQR 109–32 ppm and up to 1070 ppm In; IQR 62–1.5 ppm and up to 630 ppm Ga). In coeval generations of sphalerite and chalcopyrite, the contents of In and Ga in sphalerite are at least two times higher than in chalcopyrite. Germanium content is generally low in the four analyzed minerals (IQR 1.2–0.19 ppm), although late Fe-poor sphalerite may yield much higher values (IQR 129–74 ppm).

Certain trace element contents appear to correlate with (i) the evolving characteristics of the hydrothermal fluids during individual mineralization events, and (ii) the location of the studied ore bodies relative to the hydrothermal feeders. The highest In values in sphalerite are found in high-sulfidation assemblages in Cordilleran polymetallic veins and, with lower amounts, in low-sulfidation assemblages in skarn bodies. In intermediate-sulfidation assemblages in Cordilleran mineralization, In content decreases from early to late generations of sphalerite, while that of Ge increases. Spatial trace-element trends in Cordilleran veins and replacement bodies formed during the so-called “Morococha district-scale polymetallic event” include, from porphyry-distal to porphyry-proximal locations: i) In and Cu, and to a lesser extent Ga, enrichment in sphalerite; ii) Se and Hg enrichment and Sn and Ag depletion in chalcopyrite; iii) In enrichment in galena; and iv) Ag depletion in tetrahedrite-tennantite.

Our dataset suggests that In is incorporated in the sphalerite crystal lattice via coupled substitutions involving Cu and subordinately also Sn and Ag. Availability of Cu in the mineralizing fluids is therefore key to In enrichment in sphalerite. Progressive dilution of metal-rich magmatic-hydrothermal fluids and Cu precipitation probably account for the progressive In depletion in distal-to-porphyry Zn-Pb-Ag and Ag-Pb Cordilleran polymetallic mineralization and in late sphalerite generations in intermediate-sulfidation assemblages.

1. Introduction

Porphyry Cu systems host the world’s largest resources of Cu and Mo and are important suppliers of Au, Ag, Zn, and Pb. Formed at convergent plate margins and genetically associated with subduction- and post-subduction-related [magmatism](#), these systems host a variety of genetically connected mineralization types ([Richards, 2009](#), [Sillitoe, 2010](#), [Lee and Tang, 2020](#)). Indeed, porphyry Cu deposits, which are centered on porphyry intrusions emplaced in the upper 4 km of the crust, may be laterally and vertically associated with skarn and low-, intermediate-, and high-sulfidation epithermal polymetallic and precious metal mineralization.

Several technological or *high-tech* elements lacking primary ores may concentrate in porphyry Cu systems. Porphyry Cu (including the subtype Cu-Mo) deposits are major sources of Se, Te, and Re, which are recovered as byproducts, and may occasionally host recoverable amounts of In ([John and Taylor, 2016](#)). As for skarn deposits, those of the Au type are typically enriched in Te, whereas those of the Zn, Sn, and W types may host relatively high content of In ([Meinert, 2005](#), [Cook et al., 2009](#), [Bauer et al., 2019a](#), [Korges et al., 2020](#)). Polymetallic [epithermal deposits](#) may also display positive anomalies of Te, In, Ge, and Ga that, in some cases, can be recovered as byproducts ([Cook et al., 2009](#), [Goldfarb et al., 2016](#), [Sahlström et al., 2017](#), [Liu et al., 2019](#)). [Frenzel et al. \(2017\)](#) quantified the contribution of high-temperature carbonate replacement and vein-type deposits to the global supply potential for In in about 25%. Of these potential *high-tech* byproducts, Re is mainly found as ReS₂ in solid solution with [molybdenite](#), whereas Te usually forms a plethora of Au-Ag(-Pd) [telluride](#) minerals. The In, Ge, and Ga triad, which is the main focus of the present study, rarely forms own mineral phases but are commonly incorporated in the structure of major [sulfides](#), chiefly sphalerite and chalcopyrite (see [Cook et al., 2009](#), [Cook et al., 2011a](#), [Cook et al., 2011b](#), [Cook and Ciobanu, 2015](#), [George et al., 2018](#) for comprehensive reviews on substitution mechanisms) and, in the case of Ga, also in the structure of Al-rich hydrothermal phases such as hypogene [alunite](#) and [dickite](#) ([Rytuba et al., 2003](#), [Sahlström et al., 2017](#)).

[Indium](#) ([Reich and Richter, 1863](#)), Ge ([Winkler, 1886](#)), and Ga ([Le coq de Boisbaudran, 1875](#)) are currently considered of strategic importance and classified as critical to the health of the global economy ([Wood and Samson, 2006](#), [Skirrow et al., 2013](#), [European Commission, 2017](#), [Schulz et al., 2017](#)). This is partly explained by their increased use in both modern digital technologies and the so-called green technologies, including solar panels (In, Ge, Ga), optical electronics (In, Ge, Ga), smartphones (In, Ga), and fiber optics applications (Ge) amongst others ([Schwarz-Schampera and Herzig, 2002](#), [Guberman, 2015](#), [Jaskula, 2015](#), [Tolcin, 2015](#)). [Frenzel et al. \(2017\)](#) indicate that if the current growth in consumption continues, In could become the most problematic of the three elements in terms of future supply since most of the In contained in concentrate streams is already being extracted.

Recent work on the distribution of high-tech metals in magmatic-hydrothermal systems in the Central Andes has largely focused on xenothermal (cf. [Heuschmidt et al., 2002](#)) and epithermal deposits of the Bolivian tin belt, with well-documented conspicuous In enrichments ([Schwarz-Schampera and Herzig, 2002](#), [Murakami and Ishihara, 2013](#), [Torró et al., 2019a](#), [Torró et al., 2019b](#), [Gemmrich et al., 2021](#)). In contrast, little research has been conducted on polymetallic deposits associated with porphyry Cu systems in the region. In Peru, a comparative study of high-tech elements in [mineral deposits](#), including those framed in porphyry systems, is limited to the work carried out in zinc concentrates by [Soler \(1987\)](#) that, among other elements, reported contents of some technological elements including Cd, In, Ge, and Ga in several types of polymetallic deposits.

The present contribution documents temporal (through robust paragenetic sequences) and spatial variations in the trace-element compositions of sphalerite, chalcopyrite, galena, and tennantite-tetrahedrite in the world-class Morococha district ([Petersen, 1965](#), [Catchpole et al., 2015a](#), [Catchpole et al., 2015b](#)), Peru, with a special focus on In, Ge, and Ga. In this classical polymetallic district, several [Miocene](#) porphyry deposits including the producing Toromocho Cu-Mo porphyry (proven and probable reserves of 1474 Gt at 0.47% Cu, 0.019% Mo, and 6.89 g/t Ag; [Chinalco Mining Corporation International, 2015](#)) are associated with skarn and skarn-free (“Cordilleran”), mostly epithermal polymetallic deposits that display high-, intermediate-, and low-sulfidation mineral assemblages. Studied mineralization styles in the present work include Zn-Cu-Ag massive replacement bodies formed adjacent to, and partly overprinting, prograde exoskarn mineralization, and skarn-free Cordilleran mantos and veins spanning from veins cross-cutting the Toromocho Cu-Mo porphyry to more distal carbonate replacement bodies and veins. Minor and selected trace element compositions were determined by laser ablation inductively-coupled plasma mass spectrometry (LA-ICP-MS) with a twofold objective: i) to contextualize, temporally and spatially, the contents of In, Ge, and Ga in the different polymetallic mineralization styles; and ii) to recognize distribution patterns and district-scale zoning. The study of trace element behavior in major sulfides might also be of use to generate more optimal solutions to treat polymetallic concentrates that carry these strategic metals; prime examples of the technological implications of trace-element [mineralogy](#) are presented in [Cook et al., 2011a](#), [Frenzel et al., 2019](#).

2. Geological setting

2.1. Pre-Miocene geology

The Morococha district (11°35'S, 76°20'W) is located in the Western [Cordillera](#) of Central Peru ~ 150 km east of Lima at an altitude of 4500 to over 5000 m ([Fig. 1](#)). The district belongs to the [Eocene](#) and [Miocene](#) metallogenic belt of northern and central Peru ([Petersen, 1965](#), [Noble and McKee, 1999](#), [Bissig et al., 2008](#), [Fontboté, 2018](#)). The hydrothermal [ore deposits](#) of this belt are genetically linked to calc-alkaline [magmatism](#), ranging in age from 40 to 6 Ma. This belt hosts large [mineral deposits](#) belonging to the “porphyry system” in the sense of [Sillitoe \(2010\)](#) including porphyry Cu ± Mo ± Au (e.g., Toromocho), polymetallic and copper skarns (e.g., Antamina), epithermal (“Cordilleran”) polymetallic deposits (Cerro de Pasco, Colquijirca), and high-sulfidation epithermal gold deposits including Yanacocha.

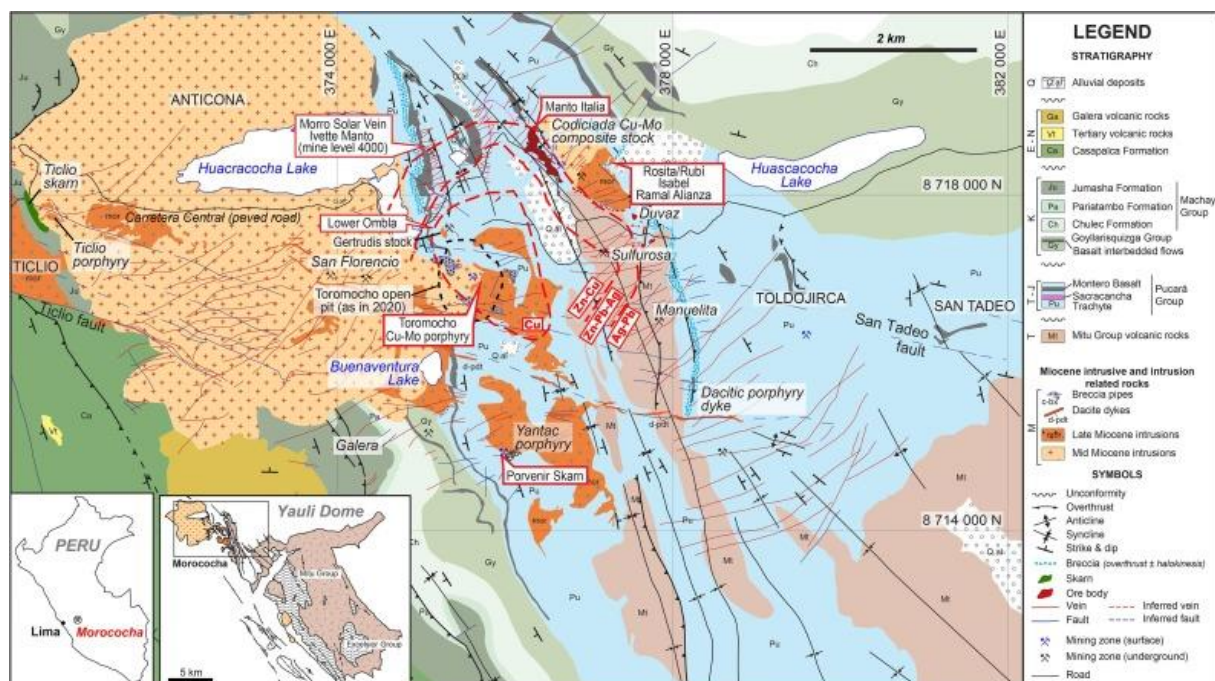


Fig. 1. Regional geologic map of the Morococha mining district (modified from [Bendezú et al., 2008](#)).

The Morococha district is located at the northern end of the northwest-trending Yauli Dome ([Petersen, 1965](#), [Catchpole et al., 2015a](#), [Catchpole et al., 2015b](#); [Fig. 1](#)). The dome comprises a core of [phyllites](#) with minor limestones, [quartzites](#), and [basalts](#) known as the Excelsior Group attributed to the [Devonian](#) ([Kobe, 1990](#), [Saintilan et al., 2021](#)). The oldest stratigraphic unit cropping out in the Morococha district consists of a ~200-m-thick sequence of interbedded red [sandstones](#) and conglomerates covered by a ~500-m-thick pile of andesitic lavas and [pyroclastic flows](#) corresponding to the rift-related Mitu Group

(Spikings et al., 2016), locally known as “Catalina volcanics” (McLaughlin, 1924, Terrones, 1949, Mégard, 1968). Age determinations (Spikings et al., 2016) and geological constraints (Rosas et al., 2007) indicate a Triassic age for the Mitu Group. The Upper Triassic to Jurassic carbonate rocks of the Pucará Group rest unconformably on the Mitu Group. The Pucará Group is subdivided, from base to top, into the Chambará, Aramachay, and Condorsinga Formations and at Morococha has an average thickness of around 450 m (Terrones, 1949, Rosas et al., 2007). At the base of the Chambará Formation, a lenticular deformed sequence of anhydrite, gypsum, shale, and limestone layers is locally known as the “anhydrite complex”. The sulfates are of evaporitic origin with local remobilization due to Miocene magmatic-hydrothermal activity (Haapala, 1953, Kouzmanov et al., 2011). The anhydrite complex is overlain by thick-bedded dolomite and subordinate limestone containing chalcedony lenses and chert nodules with intercalated shale and sandstone beds and a discontinuous ~5-m-thick lava flow, known as the Sacracancha Trachyte. The Aramachay Formation at Morococha differs from the typical black shales lithofacies of deep environment (cf. Rosas et al., 2007) by showing siliceous sponge-dominated on-shelf deposition that indicates shallow water sedimentary facies (Ritterbush et al., 2015). It comprises dolomites, shales, cherts, cherty dolomites, limestones, and intercalated tuffs hardened by sponge spicule silica remobilization which resulted in positive topography as cliffs and crests. The Condorsinga Formation displays similarities with the Chambará Formation including thick-bedded limestones with minor detrital components and chert. At Morococha, the Aramachay and Condorsinga Formations are separated by an up to 38-m-thick basaltic andesite lava flow with within-plate affinity, locally referred to as the “Montero Basalt” (Terrones, 1949, Pérez et al., 2011, Rosas et al., 1996) which constitutes an important marker horizon in the whole Yauli Dome.

The overlying Early Cretaceous Goyllarisquizga Group typically forms the flanks of the Yauli Dome and comprises red conglomerates at the base overlain by interbedded sandstones and limestones intruded by Aptian-Albian mafic sills (Terrones, 1949, Rosas, 1994). The Machay Group rocks, subdivided in Chúlec, Pariatambo, and Jumasha Formations (Lepry, 1981), rest on the Early Cretaceous rocks. Terrones (1949) described limestones, which are locally bituminous, sandstones, and marls (Chúlec Formation), finely-laminated phosphatic black carbonate rocks and lutites (Pariatambo Formation) and dolomitic limestones and limestones, overlain by alternating beds of green to red-colored shales and fossiliferous dolomitic limestone layers (Jumasha Formation). The Jumasha Formation is unconformably overlain by the Late Cretaceous to Paleocene (?) Casapalca red beds and the Galera pyroclastic flows, of rhyolitic composition, and minor proportions of undifferentiated Tertiary volcanic rocks to the southwest. Most of the folds and thrusts that characterize the Yauli Dome formed during the late Paleocene to Eocene Incaic orogenic phase (Benavides, 1999, Scherrenberg et al., 2016).

2.2. Timing of Miocene magmatic-hydrothermal activity

Mid to Late Miocene magmatic activity in the Morococha District is characterized by a succession of calc-alkaline intrusions emplaced in the afore-described Paleozoic to Cretaceous rocks. Detailed field and geochronological studies (Eyzaguirre et al., 1975, Beuchat, 2003, Kouzmanov et al., 2008, Bendeziú et al., 2012, Catchpole et al., 2015a, Catchpole et al., 2015b) allowed Catchpole et al. (2015a) to propose two main cycles of intrusion during which several successive emplacement episodes of dioritic to granodioritic magma took place. The first cycle corresponds to the emplacement of the Mid-Miocene barren microritic Codiciada intrusive in the core of the Morococha anticline at 14.3 Ma, followed by the dioritic Anticona laccolith-like body that crops out largely northwest of the district (Fig. 1). The second cycle corresponds to Late Miocene dioritic, granodioritic, and quartz monzonitic mineralized porphyry stocks emplaced between 9.4 and 7.7 Ma in the Codiciada and Anticona diorites and older rocks, followed by a late NW-SE trending dacitic dike swarm at 7.2 Ma (Fig. 1). The mineralized porphyry intrusions comprise, from NW to SE, the Ticlio, Gertrudis, Codiciada, San Francisco, Toromocho, and Yantac stocks (Fig. 1).

Based on new U-Pb, Re-Os, and $^{40}\text{Ar}/^{39}\text{Ar}$ geochronological studies and previous data, Catchpole et al. (2015a) proposed a model of multiple hydrothermal mineralization events of porphyry, skarn, and Cordilleran polymetallic deposits and ore showings that formed over a total timespan of 3.5 M.y., centered on three individual magmatic-hydrothermal centers, the oldest being the Codiciada Center (ca. 9.3 Ma), followed by the Ticlio Center (between 8.5 and 7.2 Ma), and the Toromocho Center (between 8.5 and 7.2 Ma). The Toromocho Center occupies the central part of the district, comprises several porphyry intrusions (granodiorite, quartz porphyry, feldspar porphyry, and dacitic porphyry dykes), and was responsible for the formation of the giant Toromocho porphyry Cu-Mo deposit (Kouzmanov et al., 2008).

2.3. Studied polymetallic mineralization styles in the Morococha district

In each of the Morococha centers mentioned above, porphyry and polymetallic mineralization styles have been recognized (Catchpole et al., 2015a, Catchpole et al., 2015b). The present work focuses, from old to young (all ages from Catchpole et al., 2015b and references therein), on the following polymetallic replacement bodies and veins:

- (i) Replacement bodies in “Manto Italia” (Fig. 1), emplaced subsequently to a prograde skarn phase adjacent to the Codiciada stock (ca. 9.3 Ma). Adularia $^{40}\text{Ar}/^{39}\text{Ar}$ ages (6.0 ± 0.2 Ma and 6.23 ± 0.12 Ma) of crosscutting calcite-adularia veins are interpreted by Catchpole et al. (2015b) to belong to the later hydrothermal event mentioned below under “iii”, not to the skarn-related low-sulfidation mineralization at Manto Italia;
- (ii) Porvenir skarn (7.2 ± 0.2 Ma; phlogopite $^{40}\text{Ar}/^{39}\text{Ar}$ ages), adjacent to the Yantac intrusion (ca. 8.8–8.0 Ma; Fig. 1); and
- (iii) Massive replacement bodies (mantos) and veins postdating the porphyry mineralization at Toromocho (ca. 6.8 Ma). They include veins overprinting the Toromocho porphyry stock and, from proximal to distal relative to the Toromocho porphyry, the Lower Ombla manto, the Morro Solar vein, the Ivette and Rosita mantos, and the Rubí, Isabel, and Ramal Alianza veins (Table 1).

Table 1. General description of the [geological features](#) and locations of the sampled ore bodies and veins in the Morococha district.

ORE BODY/VEIN	Description	Age/Relative age (see text for details)	Evolution stage of analyzed minerals (see text for details)
MANTO ITALIA MASSIVE REPLACEMENT BODY	Polymetallic, low sulfidation mineralization-dominated replacement body in the Chambará Formation, adjacent to the Codiciada composite stock and a relictic magnesian exoskarn. Massive Zn-Pb-Ag-Cu-bearing sulfide bodies are up to 20 m thick and composed of massive pyrrhotite, Fe-rich sphalerite, and chalcopyrite.	Slightly younger than the Codiciada stock (ca. 9.3 Ma; Catchpole et al., 2015b)	A
PORVENIR SKARN	Polymetallic, low-sulfidation assemblage on hydrous skarn in the Chambará Formation. Adjacent to the Yantac intrusion. Magnesian exoskarn of serpentine-magnetite, phlogopite, tremolite, talc, and chlorite cut by dark brown sphalerite with interstitial chalcopyrite and pyrite, and late 5–10-mm-thick calcite veinlets.	7.2 ± 0.2 ($^{40}\text{Ar}/^{39}\text{Ar}$ in phlogopite; Beuchat, 2003)	A
EPITHERMAL VEINS OVERPRINTING TOROMOCHO PORPHYRY	5–10-cm-wide high-sulfidation epithermal veins composed of chalcopyrite, pyrite, and enargite and lesser proportions of Fe-poor sphalerite overprinting the Toromocho porphyry Cu-Mo mineralization.		C
LOWER OMBLA MASSIVE REPLACEMENT BODY	Polymetallic replacement body in the Chambará Formation, close and along its underlying contact with rocks of the Mitu Group. Adjacent to the Gertrudis stock. Magnesian exoskarn of serpentine-magnetite with interstitial anhydrite and occasional epidote, replaced by massive pyrrhotite, pyrite, brown sphalerite, and chalcopyrite.		C
MORRO SOLAR VEIN	N35°E 75°SE ~ 1-m-thick polymetallic vein located at the limit between the Cu and Cu-Zn zones (Catchpole et al., 2012) NW of the Toromocho magmatic-hydrothermal center. Hosted in the Chambará Formation dolomite and anhydrite. Composed of sphalerite, pyrite, quartz, chalcopyrite, orpiment, and pale pink carbonates. The Morro Solar vein is interpreted as the feeder for the Ivette massive replacement body.		C
IVETTE MASSIVE REPLACEMENT BODY	Polymetallic replacement body located in the Cu-Zn zone (Catchpole et al., 2012) around the Toromocho magmatic-hydrothermal center. Hosted within anhydrite bodies at the base of the Chambara Formation. Brown to yellow sphalerite (late generations with schalenblende texture), galena, and pyrite crystals with interstitial anhydrite, replaced by orpiment and cut by carbonate veinlets. The samples come from the zone in which the Morro Solar vein is in contact with the Ivette body.	Postdating the Toromocho porphyry (<ca. 6.8 Ma, Catchpole et al., 2015b)	C
ROSITA REPLACEMENT BODY/RUBÍ VEIN	Polymetallic replacement body and vein in the Zn-Pb-Ag zone (Catchpole et al., 2012) around the Toromocho magmatic-hydrothermal center. The Manto is hosted in carbonates of the Pucará Group and the vein cuts Pucará Group carbonates and Catalina volcanics. Pyrite, chalcopyrite, sphalerite, and galena cut by <0.5-mm-wide white to pink carbonates veinlets. Also, sub-rounded yellow sphalerite clasts (1–20 mm) showing jigsaw-fit texture are intergrown with tetrahedrite in carbonate cement.		C
ISABEL VEIN	N45°E-55°SE ~ 1.1-m-thick polymetallic vein in the Zn-Pb-Ag zone (Catchpole et al., 2012) around the Toromocho magmatic-hydrothermal center hosted by Pucará Group carbonates. Sub-rounded sphalerite clasts (1–20 mm) and fine to coarse pyrite grains appear along with white/pale pink carbonate cement.		C
RAMAL ALIANZA VEIN	N45°E-70°SE ~ 0.8-m-thick polymetallic vein in the Zn-Pb-Ag zone (Catchpole et al., 2012) around the Toromocho magmatic-hydrothermal center. Vein cuts Pucará Group		C

ORE BODY/VEIN	Description	Age/Relative age (see text for details)	Evolution stage of analyzed minerals (see text for details)
	carbonates. Breccia formed by pyrite, brown sphalerite, and galena, with pink to beige colloform carbonate cement.		

Economic mineralization in the Manto Italia, Porvenir, and Lower Ombla replacement bodies is interpreted to have developed mainly during the retrograde stage on or adjacent to magnesian [serpentine](#) – magnetite ± phlogopite and [remolite](#) – [diopside](#) – serpentine – chlorite – talc exoskarns ([Catchpole, 2011](#), [Catchpole et al., 2015a](#), [Catchpole et al., 2015b](#)). The best example of this mineralization style in the Morococha district is Manto Italia, which consists of up to 20-m-thick massive Zn-Pb-Ag-Cu-bearing [sulfide](#) bodies ([Fig. 1](#)); mineralization comprises abundant pyrrhotite, pyrite, chalcopyrite, Fe-rich sphalerite, and galena, and minor arsenopyrite hosted in the tremolite – serpentine – chlorite – talc core of the body grading to a diopside – [andradite](#) outer zone. The low-sulfidation assemblages at Manto Italia and Porvenir described by [Catchpole, 2011](#), [Catchpole et al., 2015a](#), [Catchpole et al., 2015b](#) can be compared to “Stage A” assemblages as described in Cerro de Pasco and other Cordilleran deposits ([Rottier et al., 2016](#), [Rottier et al., 2018](#), [Fontboté, 2020](#)). Less abundant in these skarn-associated replacement bodies are paragenetically later intermediate-sulfidation assemblages containing pyrite, Fe-moderate sphalerite, tetrahedrite-tennantite, and Mn-Fe carbonates, which are best represented in the studied samples from Lower Ombla (samples from low-sulfidation assemblages from the Lower Ombla skarn were not analyzed).

Extensive steeply dipping NNE- to ENE-trending Cordilleran polymetallic veins emplaced subsequently to the Toromocho porphyry were grouped by [Catchpole et al. \(2015a\)](#) as the “Morococha district-scale polymetallic event” and dated at 5.78 ± 0.10 and 5.72 ± 0.18 Ma ($^{40}\text{Ar}/^{39}\text{Ar}$ ages). The polymetallic veins overprinting the Toromocho porphyry stock, the Morro Solar, Ramal Alianza, Isabel, and Rubí polymetallic veins as well as the Rosita and Ivette polymetallic bodies belong to this event ([Fig. 1](#)). A marked base metal zoning around the Toromocho magmatic-hydrothermal center with a Cu-rich core, a Zn-Cu intermediate zone, and outer Zn-Pb-Ag to Ag-Pb envelopes was early recognized ([McLaughlin and Graton, 1935](#), [de Pasco and Corporation, 1948](#), [Petersen, 1965](#), [Titely, 1993](#), [Catchpole et al., 2012](#); [Fig. 1](#)). The veins, mainly metric in thickness, have vertical extension reaching more than 1000 m below present-day surface. They crop out at the highest elevations in the district (5100 m) and some of them have been recognized underground at 3700 m.a.s.l. and remain open to depth. The replacement bodies are mainly found within the Pucará carbonate rocks, in particular along [thrust faults](#) and at the intersections of veins and lithological contacts.

The studied Cordilleran polymetallic veins and replacement bodies of the Toromocho Center consist mainly of mineral assemblages conforming to those described by [Catchpole et al., 2011](#), [Catchpole et al., 2015b](#). These authors subdivided the polymetallic mineralization sequence into the following generations. Quartz and pyrite ± [hematite](#) were deposited as filling of veins with sericite halos during a barren stage that can be compared to “Stage B” assemblages of [Rottier et al., 2016](#), [Rottier et al., 2018](#), [Fontboté, 2020](#). The subsequent mineral assemblages are comparable to those of “Stage C” described by these authors. They outline several sub-stages including Zn, Pb, Ag, and Cu minerals, chiefly chalcopyrite, Ag-bearing tetrahedrite-tennantite series minerals, Fe-poor sphalerite, and galena, which are commonly postdated by [rhodochrosite](#) and quartz with subordinate complex Ca-Mg-Fe-Mn carbonates, and [barite](#). The inner zones tend to show assemblages of high to intermediate sulfidation states, compared to the outer ones (intermediate to low), explaining the large mineralogical variations of this stage and the typically zoned character of the Cordilleran polymetallic veins and bodies.

Massive pyrite bodies occur as replacement of carbonate rocks and develop mainly along the lithological boundary between the Mitu and Pucará Groups, and less frequently along the brecciated contact between porphyry intrusions and carbonate rocks or as sub-vertical pipe-like bodies overprinting overthrust faults. They are predominantly made up of coarse- to fine-grained pyrite with banded texture, the remainder being mainly quartz and subordinate [rutile](#) ([Catchpole, 2011](#)). Intrusive and volcanic rocks along the contacts of these bodies show sericitic alteration. Although pyrite bodies are generally barren, they are important exploration targets as they, in places, acted as trap for Zn-Pb-Ag-Cu sulfide mineralization, in particular when crosscut by later base metal veins. The Morococha massive pyrite bodies can be compared to the “Stage B” pyrite-quartz body in Cerro de Pasco ([Rottier et al., 2016](#), [Rottier et al., 2018](#)).

Since mineral assemblages of individual polymetallic ore-bodies and veins at Morococha show characteristics and evolution that can be compared to those observed in Cerro de Pasco and in other porphyry-related polymetallic deposits, we use hereinafter the three-stage terminology proposed by [Rottier et al., 2016](#), [Rottier et al., 2018](#) and generalized by [Fontboté \(2020\)](#). In a very summarized way, Stage A is characterized by low-sulfidation mineral assemblages bearing pyrrhotite and Fe-rich sphalerite; Stage B consists basically of coarse-grained pyrite and quartz with sericite alteration; Stage C in its inner part may have high-sulfidation assemblages (typically including enargite and Fe-poor sphalerite) but mostly consists of intermediate-sulfidation assemblages including Fe-moderate to Fe-poor sphalerite, tennantite-tetrahedrite and other [sulfosalts](#), and Mn-Fe carbonates. It must be stressed that the mineral assemblages of stages A, B, and C represent steps in the evolution of single events or [ore bodies](#) but they do not imply any temporal correlation between different deposits or orebodies that, in addition, at Morococha have been formed in different periods over a time span of 3.5 M.y. The stages recognized in each studied ore body and vein are included in [Table 1](#).

[Fluid inclusion](#) and stable and radiogenic isotope studies ([Moritz et al., 2001](#), [Ageneau, 2008](#), [Kouzmanov et al., 2011](#), [Catchpole et al., 2011](#), [Catchpole et al., 2015b](#)) suggest that the Cordilleran polymetallic orebodies at Morococha formed by precipitation from intermediate-density (<5 wt% NaCl equiv.) magmatic fluids during cooling below 400 °C, accompanied by phase separation (CO₂ loss and local [salinity](#) increase). Mixing with [meteoric waters](#) occurred late in the hydrothermal history of the Morococha district during the post-sulfide carbonate stage of mineralization.

3. Materials and methods

3.1. Sampling

Sampling was conducted on drill cores and mine adits. The study is based on 64 key samples from: i) Stage A low-sulfidation mineral assemblages from the Porvenir and Manto Italia polymetallic replacement bodies; ii) Stage C high-sulfidation veins overprinting the Toromocho porphyry, and iii) Stage C intermediate-sulfidation mineral assemblages from the Lower Ombla, Morro Solar, Ivette, Ramal Alianza, Isabel, and Rosita/Rubí veins and replacement bodies (groups *ii* and *iii* listed in a roughly proximal to distal position relative to the Toromocho porphyry). The main features of the sampled [ore bodies](#) and veins are summarized in [Table 1](#). A list of the samples and details on their locations are given in [Table S1 in the Supplementary Material](#). The approximate location of the sampled sites in the geological framework of the Morococha district is shown in [Fig. 1](#). A total of 60 thick polished sections were prepared at the QEMSCAN laboratory of the Pontifical Catholic University of Peru (PUCP) and subsequently studied by optical reflected-light microscopy. A selection of 20 samples was examined on an environmental scanning [electron microscope](#) (ESEM) Thermo Fisher Quanta 650 FEI equipment with an EDAX-Octane Pro EDS [microanalysis](#) system at Centro de Caracterización de Materiales of the PUCP (CAM-PUCP). The operating conditions were 20 kV accelerating voltage and 5nA beam current in backscattered electron (BSE) imaging mode.

3.2. Electron probe micro analysis (EPMA)

Analyses of the major element composition of sulfide and tetrahedrite-tennantite series minerals were performed using a five-channel JEOL JXA-8230 electron microprobe housed at Centres Científics i Tecnològics of the University of Barcelona (CCiT-UB). The instrument was operated at 20 kV acceleration voltage, 20nA beam current, and with a beam diameter of 5 μm . Analytical standards and emission lines used for analyses were as follows: sphalerite (Zn, and S, $K\alpha$), chalcopyrite (Cu, $K\alpha$), FeS_2 (Fe, $K\alpha$), PbS (Pb, $M\alpha$), CdS (Cd, $L\beta$), GaAs (As, $L\beta$; Ga, $K\alpha$), In_2Se (In, $L\beta$), Ag (Ag, $L\alpha$), Sb (Sb, $L\alpha$), Sn (Sn, $L\alpha$) and Ge (Ge, $K\alpha$). Other measurement parameters, detection limits (d.L.) for each element, representative analyses of the different minerals investigated, and the normalization constants used for formula calculations are reported in [Table S2 in Supplementary Material](#).

3.3. Laser ablation-inductively coupled plasma-mass spectrometry (LA-ICP-MS)

Analyses of sphalerite and chalcopyrite trace element content were carried out at ETH Zürich, Switzerland by [laser ablation](#) – inductively coupled plasma – sector field – mass spectrometry (LA-ICP-SF-MS) using a RESOLUTION S-155 (ASI/Applied Spectra) 193 nm ArF [excimer laser](#) system attached to an Element XR (Thermo) sector-field ICP-MS. We used a laser repetition rate of 3 Hz, a spot diameter of 19 μm , and a laser [energy density](#) on a sample of ca. 2.5 $\text{J}\cdot\text{cm}^{-2}$. The sample surface was cleaned immediately before each analysis by three pre-ablation pulses. Ablation was performed in a dual-volume, fast-washout S-155 ablation cell (Laurin Technic) fluxed with carrier gas consisting of ca. 0.5 $\text{L}\cdot\text{min}^{-1}$ He and make-up gas consisting of ca. 1 $\text{L}\cdot\text{min}^{-1}$ Ar and 2 $\text{mL}\cdot\text{min}^{-1}$ N_2 . The ablated aerosol was homogenized via flushing through a squid device before being introduced in the plasma.

The ICP-MS instrument is equipped with a high capacity (80 $\text{m}^3\cdot\text{h}^{-1}$) interface pump to achieve a detection efficiency (based on U in NIST SRM612 glass) in the range of 2% ([Guillong et al., 2020](#)). The instrument was optimized for maximum sensitivity on the entire mass range while keeping the production of oxides low ($^{248}\text{ThO}^+ / ^{232}\text{Th}^+ \leq 0.15\%$) and the U/Th ratio at ca. 1 (on NIST SRM612 glass). The list of analyzed isotopes and corresponding dwell times is provided in [Table S3 in Supplementary Material](#). A total of 68 mass scans (ca. 0.72 s sweep time each) were acquired over ca. 50 s measurement (25 s of background measurement followed by 25 s of sample ablation).

For trace element analyses in galena and tetrahedrite-tennantite, we used a Coherent Compex Pro 102-F 193 nm ArF excimer laser system attached to a NexION 2000 [quadrupole](#) ICP-MS. Ablation was performed in a single-volume Plexiglas custom cell fluxed with carrier gas consisting of ca. 1.0 $\text{L}\cdot\text{min}^{-1}$ He. Make-up gas consisting of ca. 1 $\text{L}\cdot\text{min}^{-1}$ Ar was admixed downstream of the ablation cell. We have used the same set of ablation parameters as for other sulfide analyses, except for a larger spot diameter (30 μm). The ICP-MS instrument was optimized to fulfill the same requirements as mentioned above, except for a higher oxide production rate (relaxed to $^{248}\text{ThO}^+ / ^{232}\text{Th}^+ \leq 0.5\%$) considering the different design of the ablation cell. We have used the same list of elements as above but different dwell times (see details in [Table S3 in Supplementary Material](#)). A total of 110 mass scans (ca. 0.59 s sweep time each) were acquired over ca. 65 s measurement (40 s of background measurement followed by 25 s of sample ablation).

The resulting intensities were subsequently processed offline with the standalone version 1.3.2 of the SILLS program ([Guillong et al., 2008](#)). The sulfide pressed pellet MASS-1 (former PS-1; [Wilson et al., 2002](#)) was used as the primary reference material for trace element quantification and instrumental drift correction using conventional standard-sample bracketing. The contribution of the isobaric ^{115}Sn signal on ^{115}In has been subtracted. The Cu (for chalcopyrite and tetrahedrite-tennantite), Zn (for sphalerite), and Pb (for galena) content obtained by electron microprobe analyses were used as internal standards for relative sensitivity corrections. The data are reported in [Table S4 in Supplementary Material](#) and content statistical data are shown in [Table 2](#), [Table 3](#), [Table 4](#), [Table 5](#).

The analytical reproducibility was checked by repeated measurements of the GSD-1G ([Guillong et al., 2005](#)) and NIST SRM610 ([Jochum et al., 2011](#)) glass reference materials, and ranges from 10 to 30% relative (2σ) for most elements. The quoted uncertainties for each analysis correspond to the internal (2σ) statistical error and analytical reproducibility propagated by quadratic addition. Accuracy was controlled by repeated measurements of the UQAC-FeS-1 sulfide pressed pellet (unpublished data from D. [Savard, UQAC, 2018](#); see also [Baumgartner et al., 2020](#)).

A significant effort was made to report only the content of elements whose variations respond to solid solutions and not to mixed mineral analyses (e.g., presence of nano- and micro-inclusions) by selecting only flat, stable signal intervals in the LA-

ICP-MS spectra. The results (reported in [Table S4 in Supplementary Material](#)) show that the measurements are accurate within the calculated uncertainties.

4. Mineral assemblages

Petrographic observations are provided below for selected samples hosting the studied minerals in i) Stage A-dominated assemblages of Porvenir and Manto Italia massive replacement bodies, ii) Stage C high-sulfidation assemblages of epithermal veins overprinting the Toromocho porphyry, and iii) Stage C, intermediate-sulfidation dominated assemblages of Lower Ombla, Morro Solar, Ivette, Rosita/Rubí, Isabel, and Ramal Alianza veins and massive replacement bodies. [Figs. S1 and S2](#) illustrate textural and mineral characteristics of selected typical samples of these sites.

4.1. Stage a low-sulfidation assemblages

Manto Italia massive replacement body. The [mineralogy](#) and textures of the Manto Italia polymetallic replacement body are described in detail by [Catchpole et al. \(2015b\)](#). In the studied samples, relict magnesian exoskarn is overprinted by an assemblage dominated by pyrrhotite and sphalerite. Relict anhedral magnetite ([Fig. 2A](#)) and subhedral prismatic and pseudorhombic crystals of arsenopyrite were partly replaced by massive pyrrhotite, sphalerite, and chalcopyrite. Two generations of sphalerite were distinguished (sl_{A1} and sl_{A2}), both being Fe-rich (between 11.0 and 7.56 wt%; [Table 2](#)). The first, sl_{A1}, shows “chalcopyrite disease” ([Barton and Bethke, 1987](#)) texture ([Fig. 2B-C](#)), whereas the second, sl_{A2}, mostly lacks mineral inclusions ([Fig. 2A, G](#)). Chalcopyrite also occurs intergrown with sphalerite ([Fig. 2H](#)). Pyrrhotite is replaced by Stage B anhedral aggregates of marcasite and pyrite ([Fig. 2F-G, I](#)) and subhedral pyrite ([Fig. 2E, H](#)). Locally, minor stannite, native [bismuth](#), and bismuthinite occur as inclusions in pyrrhotite, second-generation sphalerite (sl_{A2}), and galena ([Fig. 2D, J-K](#)).

Porvenir massive replacement body. The polymetallic mineralization in this replacement body consists of a low-sulfidation mineral assemblage overprinting a magnesian skarn of serpentinite-magnetite, [phlogopite](#), [tremolite](#), talc, and chlorite ([Figs. S1A-B](#)). Magnetite grains are <1.2 mm in size. The skarn assemblage is cut by massive Fe-rich (up to 11.1 wt%; [Table 2](#)) sphalerite veins containing also local dissemination of chalcopyrite (<50 μm) and blebs of intermediate product ([Ramdohr, 1980](#)) after pyrrhotite and relicts of pyrrhotite as inclusions in pyrite ([Fig. 2L](#)). A paragenetic sequence for Porvenir is available in [Catchpole \(2011\)](#).

4.2. Stage C high-sulfidation veins overprinting the Toromocho porphyry mineralization

The studied Cordilleran polymetallic veins overprinting the Toromocho porphyry crosscut a stockwork mineralization of quartz – chalcopyrite ± chalcocite, quartz – pyrite, and quartz – pyrite – molybdenite veinlets occurring in rocks affected by potassic alteration composed primarily of [biotite](#) and minor proportions of K-feldspar, and by phyllic alteration, which is dominantly composed of white [mica](#), quartz, and pyrite ([Kouzmanov et al., 2008](#)). The ore mineralogy of the studied Cordilleran veins is dominated by Stage B anhedral to subhedral individual crystals and aggregates of pyrite <380 μm in diameter, which are overprinted by a Stage C high-sulfidation assemblage consisting of massive Cu sulfides and sulfosalts and Fe-poor (up to 231 ppm; [Table 2](#)) sphalerite replacing or growing along grain boundaries, interstices, and porosity of pyrite ([Figs. S1C-D](#)). The main Cu minerals are bornite, chalcopyrite ([Fig. 3A-B](#)), sub-rounded stannoidite <300 μm in diameter ([Fig. 3B](#)), and anhedral enargite (<1050 μm) and tennantite (<900 μm) grains ([Fig. 3C-D](#)). The occurrence of chalcopyrite in these veins would point to the occasional passage from high- to intermediate-sulfidation (or vice versa) conditions during vein [emplacement](#). To a lesser extent, covellite (<50 μm), luzonite (<50 μm), and colusite (<100 μm) grains partially replaced enargite ([Fig. 3D](#)). Local euhedral to subhedral prismatic hübnerite grains <510 μm long occur as inclusions in quartz and pyrite ([Fig. 3C](#)). Scarce galena grains <50 μm in size are present as disseminations in sphalerite, enargite/luzonite, and tennantite ([Fig. 3D](#)). Bladed molybdenite crystals <200 μm in length ([Fig. 3E](#)) and anhedral grains of wittichenite (<50 μm; [Fig. 3F](#)) are found enclosed in sphalerite and pyrite, respectively.

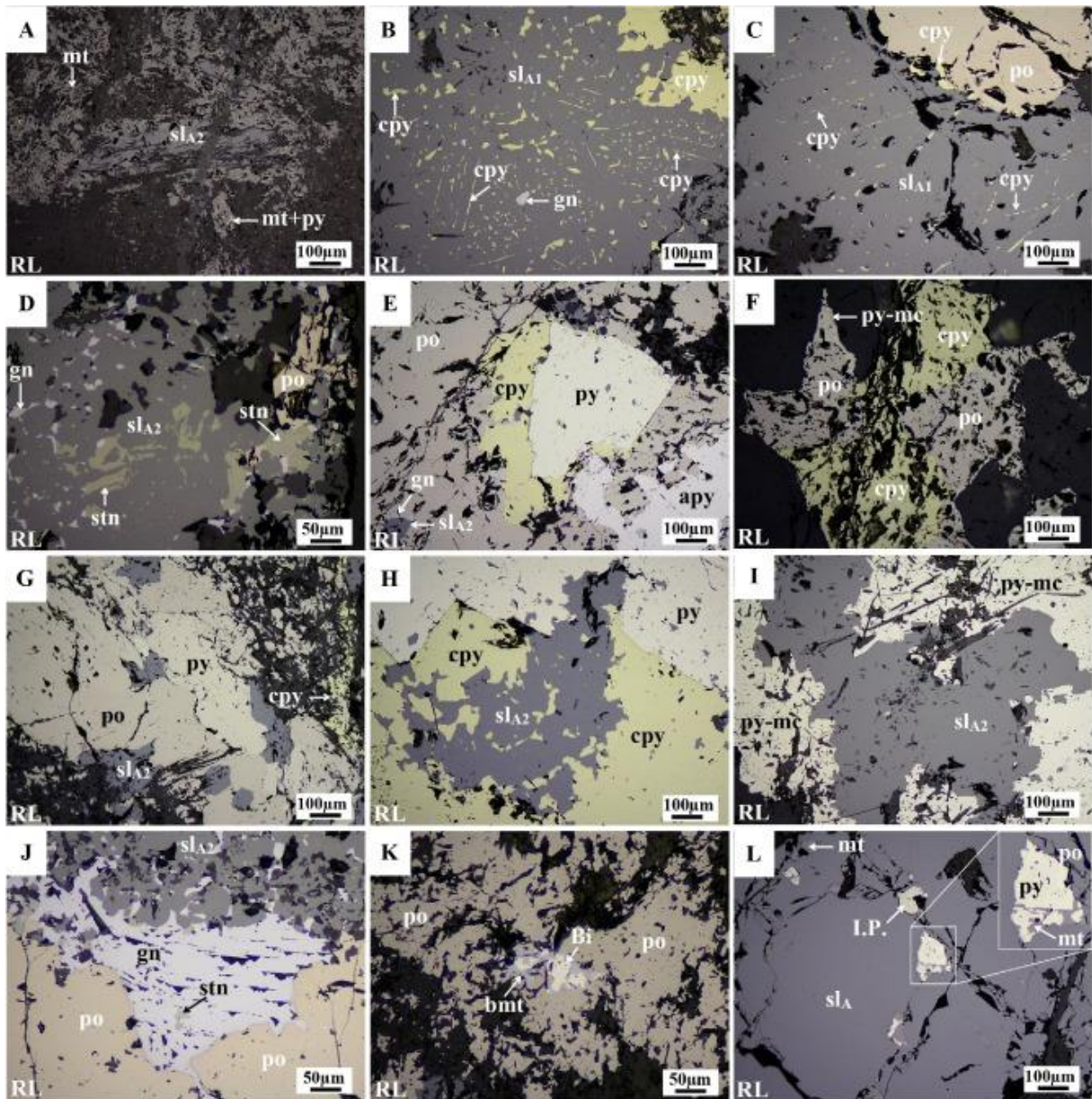


Fig. 2. *Photomicrographs* of textural features in Manto Italia (A-K) and Porvenir (L). A) Anhedral magnetite replaced by sphalerite (sl_{A2}). B) Sphalerite (sl_{A1}) with dissemination of chalcopyrite and intergrown with massive chalcopyrite. C) Pyrrhotite replaced by sphalerite (sl_{A1}) with chalcopyrite. D) Sphalerite (sl_{A2}) with inclusions of galena and partly replaced by stannite. E) Chalcopyrite as replacement of pyrrhotite, pyrite, and arsenopyrite. F) Massive pyrrhotite replaced by chalcopyrite. G) Pyrrhotite replaced by pyrite, sphalerite (sl_{A2}), and chalcopyrite. H) Chalcopyrite intergrown with sphalerite (sl_{A2}) in contact with anhedral pyrite. I) Massive sphalerite (sl_{A2}) replaced by pyrite and marcasite. J) Galena as replacement of pyrrhotite and sphalerite (sl_{A2}). K) Massive pyrrhotite with inclusions of bismuthinite and native bismuth. L) Magnetite pervasively replaced by sphalerite, with small inclusions of pyrite, intermediate product, and hematite after pyrrhotite. Abbreviations: apy: arsenopyrite; Bi: native bismuth; bmt: bismuthinite; cc: calcite; cpy: chalcopyrite; gn: galena; hm: hematite; I.P.: intermediate product; mt: magnetite; mc: marcasite; po: pyrrhotite; py: pyrite; stn: stannite; sl: sphalerite; RL: reflected light image.

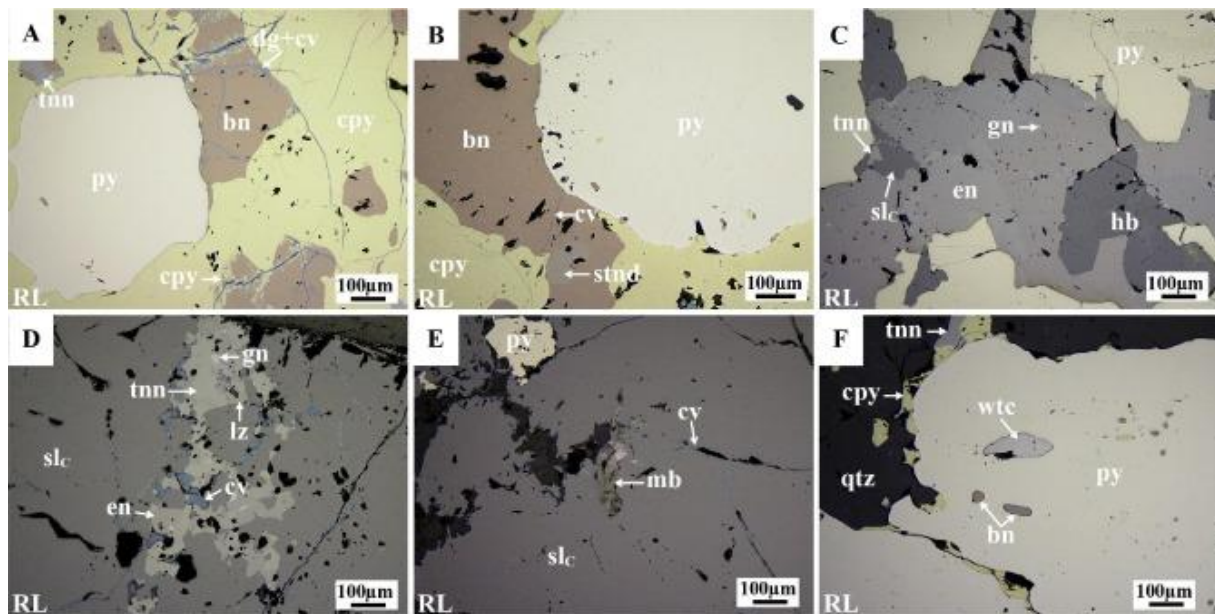


Fig. 3. *Photomicrographs* of textural features in epithermal veins overprinting the Toromocho *porphyry*. A) Anhedral *pyrite* along with massive *bornite* partly replaced by *chalcopyrite* along fractures and borders. B) *Pyrite* replaced by *chalcopyrite* and *bornite*, the latter with an inclusion of *stannoidite* and cut by *covellite* veinlets. C) *Pyrite* with *hübnerite* inclusions replaced by *enargite*, *sphalerite*, *galena*, and *tennantite*. D) Massive *sphalerite* cut by *tennantite*, *enargite*, *luzonite*, and *covellite*. Fine inclusions of *galena* in both *sphalerite* and *sulfosalts* are observed. E) *Sphalerite* with inclusions of *molybdenite* and cut by *covellite* veinlets. F) *Chalcopyrite* around *pyrite* grains, which host inclusions of *bornite* and *wittichenite*. Abbreviations: bn: *bornite*; cpy: *chalcopyrite*; cv: *covellite*; en: *enargite*; gn: *galena*; hb: *hübnerite*; lz: *luzonite*; mb: *molybdenite*; py: *pyrite*; sl: *sphalerite*; stnd: *stannoidite*; tnn: *tennantite*; wtc: *wittichenite*; RL: *reflected light image*.

4.3. Stage C intermediate-sulfidation assemblages in Cordilleran veins and replacement bodies

4.3.1. Lower Ombla massive replacement body

(*not to be confused with the classical Ombla ore body – *type locality* for *enargite* – which is located topographically at higher levels and comprises a high-sulfidation assemblage; see [Catchpole, 2011](#)). In the Lower Ombla ore body ([Table 1](#)), magnesian serpentine-magnetite exoskarn with *interstitial* anhydrite and local *epidote* is overprinted by low- and intermediate-sulfidation polymetallic assemblages ([Figs. S1E–H](#)). Only minerals belonging to intermediate-sulfidation assemblages have been analyzed in this study. Magnetite occurs as micro-fractured subhedral to anhedral crystals <950 µm in diameter partly replaced by sulfides ([Fig. 4A–D](#)). Locally, abundant Stage A massive pyrrhotite is replaced by Stage B pyrite and marcasite. Stage C chalcopyrite and Fe-poor (up to 3.59 wt%; [Table 2](#)) sphalerite occur as a replacement of pyrrhotite and pyrite along grain boundaries and fractures ([Fig. 4E, H](#)). A first generation of sphalerite (sl_{c1}) forms minute (<5µm) star-shaped inclusions in first-generation chalcopyrite (cpy₁) exhibiting transformation twinning ([Fig. 4B](#)) as well as massive aggregates with reddish-brown internal reflections and abundant disseminations of chalcopyrite blebs (“chalcopyrite disease” texture; second-generation chalcopyrite – cpy₂; [Fig. 4E–F](#)). A second generation of sphalerite (sl_{c2}) occurs as grains without or with only limited “chalcopyrite disease” and shows orange to yellowish-brown internal reflections ([Fig. 4D–G](#)). Pyrrhotite, pyrite, and first-generation sphalerite (sl_{c1}) were replaced by second-generation chalcopyrite (cpy₂), which does not show transformation twinning ([Fig. 4H](#)). Pyrite aggregates and second-generation chalcopyrite (cpy₂) are intergrown with, and their porosity filled with, bornite (<170 µm), wittichenite (<60 µm), and bismuthinite (<270 µm; [Fig. 4J–L](#)). Rare tetrahedrite-tennantite grains <220 µm in diameter with fine dissemination of tsumoite (<60 µm) were found ([Fig. 4I](#)).

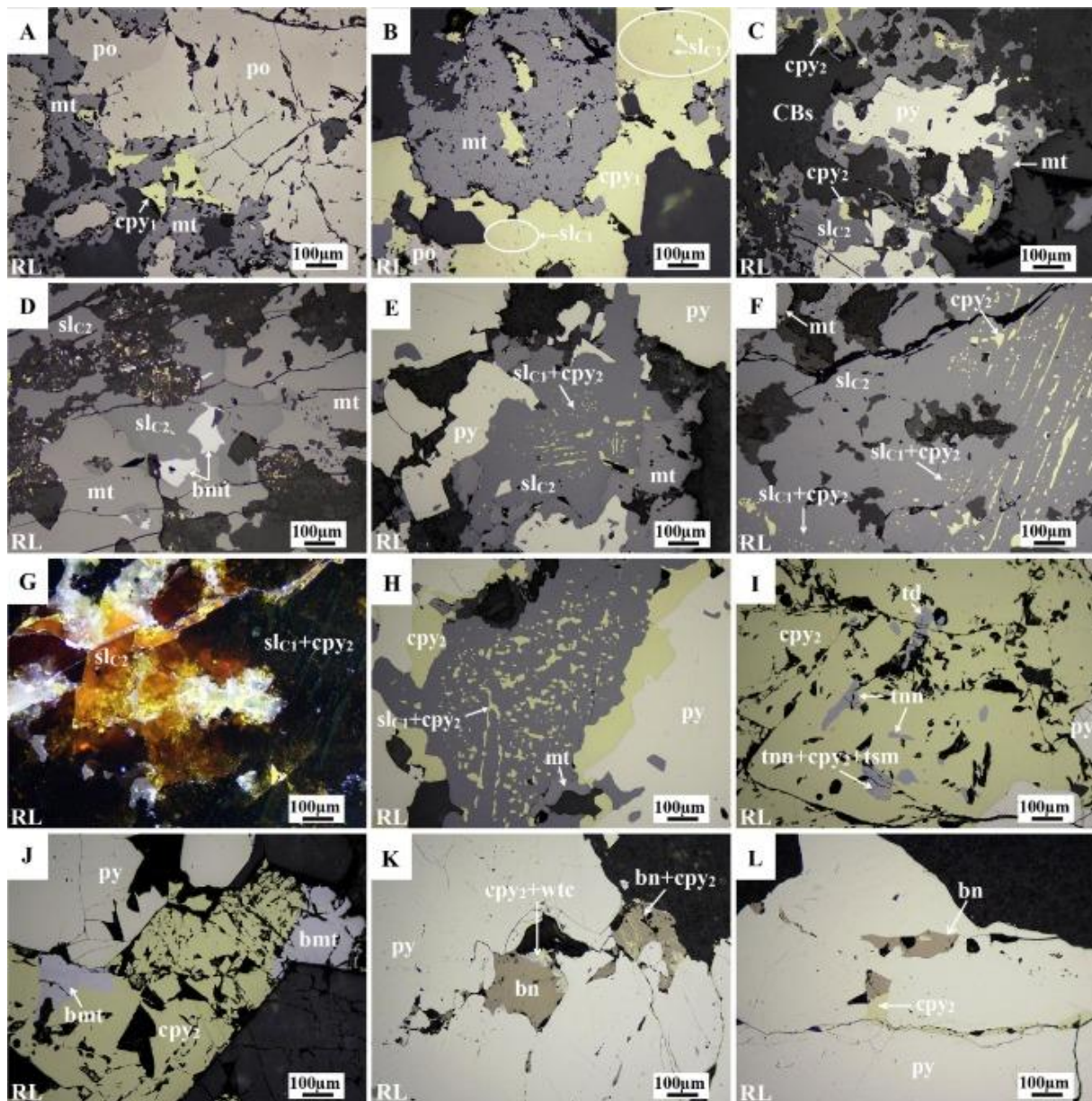


Fig. 4. Photomicrographs of textural features in the Lower Ombla massive replacement body. A-B) Anhedra magnetite replaced by massive pyrrhotite and chalcopyrite (cpy₁) with some star-like inclusions of sphalerite (slc₁). C) Magnetite replaced by pyrite, chalcopyrite (cpy₂), and sphalerite (slc₂). D) Magnetite replaced by sphalerite (slc₂) and bismuthinite. E) Magnetite and pyrite crystals replaced by sphalerite (slc₁) with chalcopyrite as fine disseminations and inclusions (cpy₂). F-G) Parallel and crossed nicols images of sphalerite (slc₁) with “chalcopyrite disease” texture overgrown by sphalerite (slc₂) with clean surfaces. Note that both generations of sphalerite show contrasting internal reflection colors. H) Replacement of pyrite and sphalerite (slc₁) by chalcopyrite (cpy₂). I) Chalcopyrite (cpy₂) with inclusions of tennantite and fine disseminations of tsumoite. J) Pyrite aggregates and chalcopyrite (cpy₂) replaced by bismuthinite. K) Pyrite with cavities lined with bornite, chalcopyrite (cpy₂) and wittichenite. L) Pyrite microfractures filled with chalcopyrite (cpy₂) and bornite. Abbreviations: bmt: bismuthinite; bn: bornite; cpy: chalcopyrite; mt: magnetite; po: pyrrhotite; py: pyrite; sid: siderite; sl: sphalerite; tnn: tennantite; tsm: tsumoite; wtc: wittichenite; RL: reflected light image.

4.3.2. Rosita, Rubí, Isabel, Ramal Alianza, Morro Solar, and Ivette veins and replacement bodies.

Due to their proximity (Fig. 1) and similarity with respect to the paragenetic sequence of major sulfides and sulfosalts, the other studied replacement bodies and veins have been separated into two groups. The first group comprises the Rosita body and the Rubí vein (both sampled at the same mine level, where both structures intersect each other), and the Ramal Alianza and Isabel veins, all located at the Codiciada Center and hosted in the porphyry stock itself or rocks of the Mitu and Pucará Groups (Table 1). The second group comprises the Morro Solar vein and the Ivette replacement body, both located at the Alapampa zone and hosted in limestones of the Chambará Formation (Pucará Group). The Morro Solar vein is interpreted to be the feeder of the Ivette replacement body.

Rosita replacement body and Rubí, Isabel, and Ramal Alianza veins (Figs. S2D–G). Massive pyrrhotite (Fig. 5A–B) and local arsenopyrite define a low-sulfidation assemblage typical of Stage A. Stage B stands out by the presence of finely intergrown pyrite and marcasite as replacement of pyrrhotite (Fig. 5A–B), as well as pyrite forming subhedral to anhedra micro-fractured

crystals <60 μm in size in a matrix of quartz (Fig. 5C). Stage C has been subdivided into the Fe-Cu-Zn-As, Pb, and carbonate sub-stages. The Fe-Cu-Zn-As sub-stage is defined by precipitation of subhedral pyrite with inclusions of hematite (var. specularite), chalcopyrite, and bornite. Porosity and micro-fractures in pyrite grains are lined with sphalerite (up to 7.9 wt% Fe; Table 2), chalcopyrite, and tetrahedrite-tennantite (Fig. 5D-J). Commonly, coarse (5–10 μm) inclusions of chalcopyrite accumulate in the core of first-generation sphalerite (sl_{c1}), whereas fine (<5 μm) chalcopyrite dissemination occurs at the rim (Fig. 5F), thus producing a watermelon-like texture (Barton and Bethke, 1987). A second generation of sphalerite (sl_{c2}) lacks chalcopyrite disseminations. The mineral assemblage of the Pb sub-stage is mainly composed of galena (<500 μm), which partially replaced minerals of the previous Fe-Cu-Zn-As sub-stage. Galena hosts rare inclusions of tellurian canfieldite and hessite (Fig. 5K). The mineral assemblages of the carbonate sub-stage consist essentially of carbonates (mostly rhodochrosite) with local pyrrargyrite (<250 μm) and proustite (<50 μm) in micro-fractures (Fig. 5L). Fig. 6 shows a unified paragenetic sequence for the Rosita/Rubí, Isabel, and Ramal Alianza mineralizations.

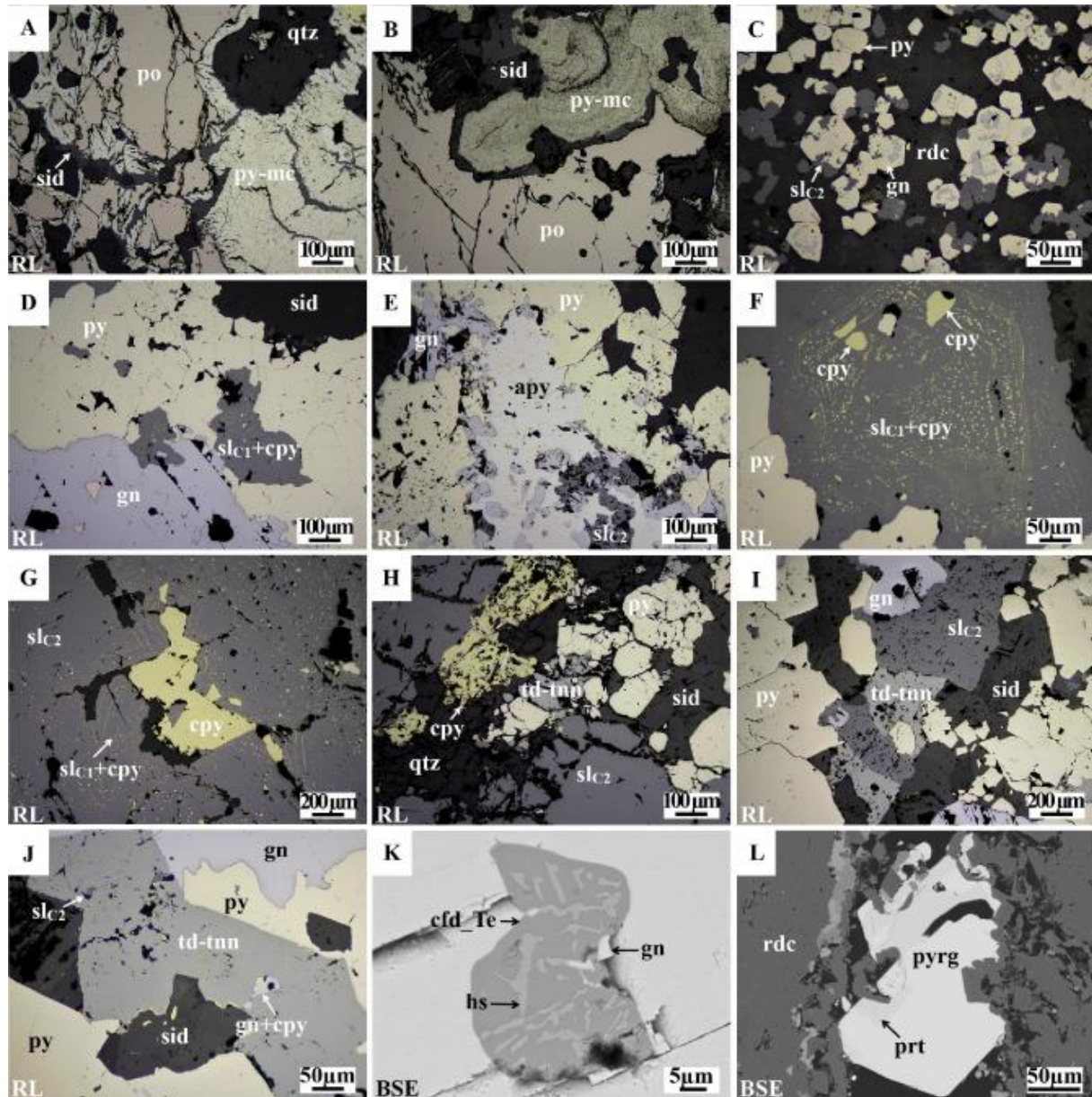


Fig. 5. Photomicrographs of textural features in the Rosita body and Rubí/Isabel/Ramal Alianza veins. A-B) Massive pyrrhotite replaced by pyrite, marcasite, and siderite in a quartz matrix. C) Subhedral pyrite aggregates replaced by sphalerite (sl_{c2}). D) Pyrite replaced by sphalerite (sl_{c1}) with fine chalcopyrite blebs, and galena. E) Pyrite replaced by arsenopyrite, sphalerite (sl_{c2}), and galena. F-G) Sphalerite (sl_{c1}) with disseminations of chalcopyrite, which also fills cavities. H-I) Pyrite aggregates replaced by sphalerite (sl_{c2}), chalcopyrite, and tetrahedrite-tennantite, in a siderite matrix. J) Pyrite replaced by galena and tetrahedrite-tennantite, with inclusions of chalcopyrite, sphalerite (sl_{c2}), and galena. K) Galena with inclusions of tellurian canfieldite and hessite. L) Pyrrargyrite-proustite crystals in micro-fracture in rhodochrosite. Abbreviations: apy: arsenopyrite; cpy: chalcopyrite; cfd_Te: tellurian canfieldite; gn: galena; hs: hessite; mc: marcasite; mlc: melnicovite; po: pyrrhotite; prt: proustite; pyrg: pyrrargyrite; py: pyrite; qz: quartz; sid: siderite; sl: sphalerite; td: tetrahedrite; tnn: tennantite; BSE: backscattered electron scanning electron microscopy image; RL: reflected light image.

Paragenetic Sequence - Rosita ore body and Rubí, Isabel and Ramal Alianza veins					
	Stage A	Stage B	Stage C		
			Pyrrhotite stage	Quartz-pyrite stage	Fe-Cu-Zn-As sub-stage
Quartz	SiO ₂	—————	—————	—————	—————
Pyrrhotite	Fe _{1-x} S	—			
Arsenopyrite	FeAsS	—		
Marcasite	FeS ₂	—————			
Pyrite	FeS ₂	—————	—————		
Hematite	Fe ₂ O ₃			
Sphalerite	ZnS		—————		
Chalcopyrite	CuFeS ₂		—		
Tetrahedrite-Tennantite series	Cu ₁₂ (Sb,As) ₄ S ₁₃		—————		
Bornite	Cu ₅ FeS ₄			
Galena	PbS			—————	
Tellurian canfieldite	Ag ₈ (Sn,Ge)(S,Te) ₆			
Hessite	Ag ₂ Te			
Proustite	Ag ₃ AsS ₃			
Pyrargyrite	Ag ₃ SbS ₃			
Rhodochrosite	MnCO ₃				—————

.....	trace	—	lesser abundant	—————	fairly abundant	—————	abundant
-------	-------	---	-----------------	-------	-----------------	-------	----------

Fig. 6. Paragenetic sequence for the Rosita ore body and the Rubí, Isabel, and Ramal Alianza veins. Thick bars indicate higher abundances and dashed lines, lesser abundances.

Morro Solar vein and Ivette replacement body (Figs. S2A–C). The first quartz-pyrite stage (corresponding to Stage B) is primarily composed of quartz and a first generation of pyrite (py₁) that forms subhedral to euhedral individual crystals <650 μm in size (Fig. 7A–B). Stage C is subdivided into the Fe-Cu-As-Sn-Zn, Zn-Pb, and carbonate sub-stages. The Fe-Cu-As-Sn-Zn sub-stage, the most widespread and economically important, is mostly composed of sphalerite, chalcopyrite, tetrahedrite-tennantite, and a second generation of pyrite (py₂) that occurs as micro-fractured subhedral to anhedral crystals <500 μm in size (Fig. 7C). Traces of hübnerite <375 μm long are enclosed in second-generation pyrite (py₂), which also contains small and abundant subrounded inclusions of sulfides, sulfosalts, and tellurides (e.g., cubanite, chalcopyrite, enargite, famatinite – var. stibioluzonite, tennantite – var. tellurian tennantite, hodrusite – Fig. S3F, stannoidite – Fig. S3D, vincienite – Fig. 7J, S3G, tellurobismuthite – Fig. S3I). First- (py₁) and second- (py₂) generation pyrite grains were replaced along grain boundaries and micro-fractures by massive sphalerite with moderate Fe content (up to 5.79 wt%; Table 2), tetrahedrite-tennantite, chalcopyrite, and galena and show rims of a third generation of distinctly porous and botryoidal pyrite (py₃; Fig. 7H). In this sub-stage, two generations of Fe-poor sphalerite (slc₁ and slc₂) were identified: i) first-generation sphalerite (slc₁) shows fine disseminations of chalcopyrite distributed along its crystallographic faces (Fig. 7D–E); ii) second-generation sphalerite (slc₂) shows no or only minor, local “chalcopyrite disease”. Sphalerite grains are commonly intergrown with massive chalcopyrite and replaced by tetrahedrite-tennantite and galena (Fig. 7E–G). Locally, second-generation sphalerite (slc₂) was also replaced by stibioluzonite (Fig. S3E) and radial aggregates of orpiment (<150 μm; Fig. S3C) while stannoidite, vincienite, aikinite, and tsumoite are found as replacement of tetrahedrite-tennantite and galena (Fig. 7I and S3H). Sulfides of the Zn-Pb sub-stage are mainly galena and a third generation of sphalerite (slc₃) forming yellowish-brown to cream-colored colloform layers (var. schalenblende; Ramdohr, 1980; Fig. 7K–L). The mineral assemblage of the carbonate sub-stage consists dominantly of siderite and intermediate members of the siderite-rhodochrosite series (var. manganosiderite), as well as quartz and anhydrite. In places, galena hosts minute inclusions of plagioclite (<10 μm), hessite (<65 μm), petzite (<25 μm), and native tellurium (<7 μm; Figs. S3A–B, J–K). Locally, minute crystals of proustite (<3 μm) and electrum (<8 μm) line porosity in siderite and anhydrite (Fig. S3L). Fig. 8 shows a unified paragenetic sequence for both the Morro Solar and Ivette ore bodies.

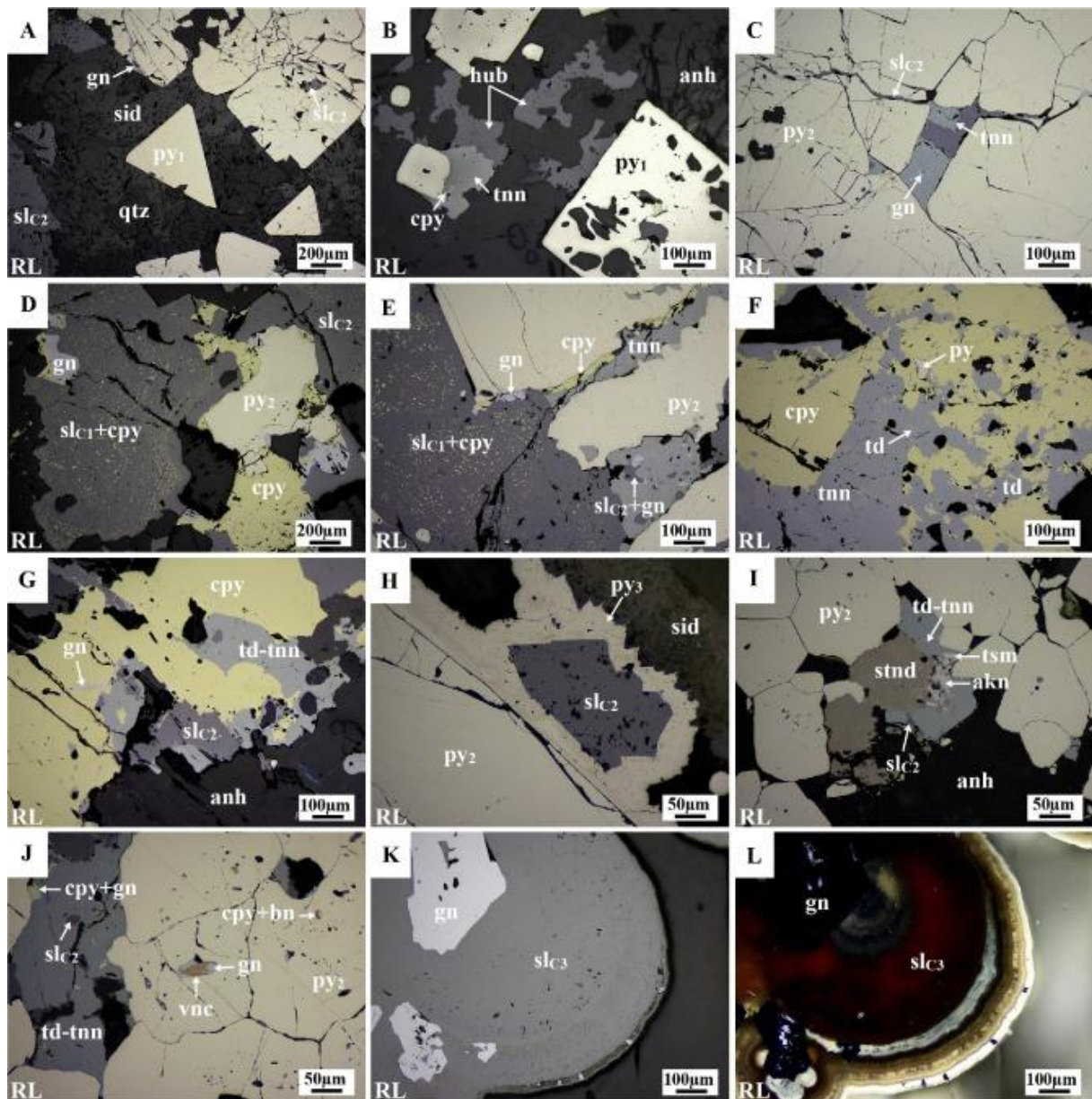


Fig. 7. Photomicrographs of textural features in the Morro Solar vein and Ivette manto. A) Pyrite (py₁) and sphalerite (slc₂) crystals on quartz and siderite matrix. Some pyrite grains present sphalerite inclusions and replacement by galena from its borders. B) Pyrite (py₁) and hübnerite crystals on a siderite and anhydrite matrix, replaced by tennantite with chalcopyrite. C) Micro-fractured pyrite aggregates (py₂) lined with sphalerite (slc₂), tennantite and galena. D-E) Anhedral pyrite (py₂) replaced by sphalerite (slc₁; with fine disseminations of chalcopyrite blebs), galena, sphalerite (slc₂), massive chalcopyrite, and tennantite. F) Massive chalcopyrite replaced by tetrahedrite and tennantite. G) Massive sphalerite (slc₂) replaced by tetrahedrite, tennantite, and chalcopyrite with inclusions of galena. H) Pyrite (py₂) and sphalerite (slc₂) wrapped by botryoidal pyrite (py₃). I-J) Pyrite aggregates (py₂) replaced by stannoidite, tetrahedrite-tennantite, galena, and chalcopyrite, with small inclusions of vincennite, galena, chalcopyrite, and bornite within an anhydrite matrix. Inclusions of aikinite, tsumoite, and sphalerite (slc₂) in tetrahedrite-tennantite are also observed. K-L) Concentric sphalerite (slc₃) bands intergrown with galena in both parallel and crossed nicols. Abbreviations: akn: aikinite; anh: anhydrite; bn: bornite; cpy: chalcopyrite; gn: galena; hb: hübnerite; py: pyrite; qz: quartz; sid: siderite; sl: sphalerite; stnd: stannoidite; td: tetrahedrite; tnn: tennantite; tsm: tsumoite; vnc: vincennite; RL: reflected light image.

Paragenetic Sequence - Morro Solar vein and Ivette ore body				
		Stage B	Stage C	
		Quartz-pyrite stage	Fe-Cu-Zn-As-Sn sub-stage	Zn-Pb sub-stage
Quartz	SiO ₂	—————		
Pyrite	FeS ₂	—————		
Sphalerite	ZnS		—————
Chalcopyrite	CuFeS ₂		—————	
Stibioluzonite-luzonite	Cu ₃ (As,Sb)S ₄		
Tetrahedrite-Tennantite series	Cu ₁₂ (Sb,As) ₄ S ₁₃		—————	
Hübnerite	MnWO ₄		
Cubanite	CuFe ₂ S ₃		
Stannoidite	Cu ₈ Fe ₃ Sn ₂ S ₁₂		
Vinciennite	Cu ₁₀ Fe ₄ Sn(As,Sb)S ₁₆		
Enargite	Cu ₃ As ₄ S ₄		
Bornite	Cu ₅ FeS ₄		
Digenite	Cu ₉ S ₅		
Covellite	CuS		
Hodrusite	Cu ₈ Bi ₁₂ S ₂₂		
Tellurobismutite	Bi ₂ Te ₃		
Galena	PbS		—————	
Aikinite	PbCuBiS ₃		
Tsumoite	BiTe		
Plagionite	Pb ₅ Sb ₄ S ₁₇		
Proustite	Ag ₂ As ₂ S ₃		
Hessite	Ag ₂ Te		
Petzite	Ag ₃ AuTe ₂		
Native Tellurium	Te		
Electrum	(Au, Ag)		
Orpiment	As ₂ S ₃			—
Siderite/Manganosiderite	FeCO ₃ /(Fe,Mn)CO ₃			—————

.....	trace	———	lesser abundant	—————	fairly abundant	—————	abundant
-------	-------	-----	-----------------	-------	-----------------	-------	----------

Fig. 8. Paragenetic sequence for the Morro Solar vein and the Ivette replacement body. Thick bars indicate higher abundances and dashed lines, lesser abundances.

5. Ore mineral geochemistry

Sphalerite, chalcopyrite, galena, and tetrahedrite-tennantite show, in general, a wide range of major and trace element contents. A summary of the compositions, including minimum, maximum, geometric mean, and interquartile range (IQR) values is reported in [Table 2](#), [Table 3](#), [Table 4](#), [Table 5](#). Content values will be hereinafter reported as the IQR unless otherwise specified. Of the analyzed elements, only Ag, Bi, and Pb in sphalerite, Pb and Bi in chalcopyrite, Mn, Cu, and Zn in galena, and Pb and Tl in tetrahedrite-tennantite present occasionally spiky LA-ICP-MS transient signals and therefore the occurrence of micro and nano-scale solid inclusions cannot be completely ruled out.

5.1. Sphalerite

Sphalerite shows a relatively wide range of Fe content ([Table 2](#)). Iron content measured with LA-ICP-MS (up to 79,760 ppm; av. = 17,411 ppm) are broadly comparable with those measured with EPMA (up to 11.1 wt%; av., 1.78 wt%; [Table 2](#)); however, Fe-rich sphalerite tends to yield lower values – up to 30% lower – with the second method. The Fe content is generally higher in sphalerite from Stage A low-sulfidation assemblages (Porvenir, 10.3–9.90 wt%; Manto Italia: first generation 10.8–8.42 wt%, and second generation, 10.8–10.1 wt%), and much lower in grains from Stage C high-sulfidation epithermal veins overprinting the Toromocho porphyry (189–85 ppm; [Fig. 9A](#)). In sphalerite from the Stage C intermediate-sulfidation assemblages, Fe is highly variable among the different studied ore bodies, in the range between 7.93 wt% and 12 ppm, and there is a pronounced Fe depletion from early to late generations ([Table 2](#), [Fig. 9A](#)).

Table 2. Summary of element contents in sphalerite from the Morococha district. Sulfur, Zn, and Fe are given in wt% (EPMA data) and all trace elements, in ppm (LA-ICP-MS data).

Geo-body/min	Generation	S	Cu	Fe	Pb	Co	Ga	Ag	Cd	Zn	Pb	Sb	Mn	Se	Mo	Cu	Au	Hg	Tl	Bi	As		
		(wt%)	(wt%)	(wt%)	(ppm)	(ppm)	(ppm)	(ppm)	(ppm)	(ppm)	(ppm)	(ppm)	(ppm)	(ppm)	(ppm)	(ppm)	(ppm)	(ppm)	(ppm)	(ppm)	(ppm)		
Entire district (n=332)	MIN	31.9	52.2	0.11	B.D.L.	B.D.L.	B.D.L.	B.D.L.	B.D.L.	0.088	0.016	1.3	0.13	B.D.L.	B.D.L.	B.D.L.	B.D.L.	B.D.L.	1.2	B.D.L.	B.D.L.	B.D.L.	
	MAX	34.7	68.4	1.11	79.560	26.259	594	4008	30	2107	71.83	82	340	11	247	52	81	202	15	291	0.80	9.9	123
	GM	33.3	64.6	0.98	1.099	184	2310	25	0.53	62	181	72	61	0.75	0.41	22	0.30	0.62	0.018	0.7	0.07	0.091	16
	QR	33.5(10)	65.5(4)	2.2(2)	10.2(3)	284(20)	801(50)	217(2)	0.8(1)	6(2)	16(1)	6(1)	3(2)	0.2(2)	0.2(2)	12(1)	0.3(2)	0.7(1)	1.7(1)	0.1(2)	0.01(1)	0.2(1)	0.7(1)
Porcaine (n=31)	MIN	32.1	54.4	7.96	45.77	2111	1669	143	0.18	0.089	1.9	2.5	0.15	0.055	B.D.L.	17	0.23	108	1.1	12	B.D.L.	0.901	8.17
	MAX	34.4	86.6	1.11	79.560	15.908	2112	217	0.57	0.27	4.06	4.8	3.2	4.9	0.29	52	1.6	262	0.91	2.6	0.05	8.5	37
	GM	33.4	58.5	8.8	75.808	878	1832	158	0.35	0.18	17.6	37	0.38	0.80	0.80	38	0.45	232	0.015	1.8	0.069	0.38	87
	QR	33.5(29)	59.5(9)	11.3(8)	75.18(2)	158(3)	2074(17)	336(11)	0.44(3)	0.24(1)	108(29)	150(18)	0.10(2)	0.027	48(35)	0.58(2)	284(7)	0.15(2)	1.2(1)	0.012(0)	0.64(1)	35(40)	
Nanta Bula (n=17)	MIN	33.8	52.2	8.42	88.01	2662	1864	19	B.D.L.	62	28	3.8	0.18	0.05	B.D.L.	B.D.L.	0.31	0.978	B.D.L.	2.1	B.D.L.	0.062	8.25
	MAX	34.3	57.4	1.11	79.560	5711	2108	71	0.25	100	845	12	0.26	1.9	0.08	1.8	0.00	0.29	0.021	4.8	0.001	0.18	4.96
	GM	34.0	56.0	5.29	47.552	4090	2408	39	0.17	46	126	3.9	0.22	1.1	0.21	1.1	0.41	0.18	0.036	3.2	0.006	0.038	8.77
	QR	34.1(19)	57.6(4)	10.4(4)	77.088(8)	5051(867)	3274(170)	68(3)	0.20(1)	140(21)	381(42)	9.6(15)	0.24(3)	1.6(3)	0.60(0)	1.5(8)	0.2(1)	0.19(0)	0.018(0)	1.2(1)	0.005(0)	0.15(0)	0.5(2)
Epithermal overprint Tirosocha porphyry (n=7)	MIN	32.8	66.6	B.D.L.	56	62	3638	145	0.08	486	1982	3.9	0.44	0.84	0.82	1.8	0.2	B.D.L.	B.D.L.	130	0.887	0.21	B.D.L.
	MAX	33.4	66.7	B.D.L.	201	548	4367	1586	42	1758	379	67	8.1	3.4	2.1	19	1.3	0.11	0.088	25	0.82	1.2	B.D.L.
	GM	33.1	66.1	-	131	206	3899	775	1.6	899	2126	4.8	1.9	1.6	0.28	6.3	0.36	0.058	0.015	179	0.819	0.45	8.85
	QR	33.1(22)	66.6(9)	-	189(8)	4075(218)	4025(710)	1281(210)	21(12)	1286(76)	3096(771)	5.8(12)	2.6(1)	1.9(4)	0.3(1)	13(1)	0.56(2)	0.066(0)	0.015(0)	195(10)	0.925(0)	0.63(1)	0.78(1)
Lower Ore (n=27)	MIN	33.8	63.3	1.06	10.800	499	1872	45	B.D.L.	0.78	5.1	28.0	0.0	B.D.L.	B.D.L.	5.3	0.090	B.D.L.	B.D.L.	42	B.D.L.	0.04	8.80
	MAX	33.3	65.4	3.24	20.002	1998	2094	77	0.47	6.5	2.7	13.4	1.3	B.D.L.	11	0.26	13	0.055	8.2	0.054	4.2	8.81	
	GM	33.4	65.3	2.99	17.209	1889	2001	85	0.28	1.9	95	2.9	1.06	0.49	-	8.1	0.15	1.0	0.067	3.7	0.049	5.5	8.70
	QR	33.3(10)	65.6(4)	3.1(1)	20.0(1)	1855(41)	1976(187)	51(2)	0.32(1)	4.2(1)	100(7)	3.2(2)	1.7(4)	0.8(1)	-	10(8)	0.24(0)	0.56(1)	0.031(0)	8.5(4)	0.067(0)	0.063	27(10)
Morococha (n=85)	MIN	32.1	64.0	B.D.L.	B.D.L.	B.D.L.	B.D.L.	B.D.L.	0.18	B.D.L.	1.3	0.20	B.D.L.	B.D.L.	B.D.L.	B.D.L.	B.D.L.	B.D.L.	B.D.L.	0.3	B.D.L.	B.D.L.	12
	MAX	34.3	87.8	1.06	5666	1974	3984	1804	708	2118	3588	82	426	11	247	5.2	4.4	0.01	1.5	288	0.8	87	690
	GM	33.3	66.1	0.19	373	33	1385	43	1.1	37	306	5.3	15	0.89	1.7	1.7	0.30	0.18	0.028	56	0.015	0.27	40
	QR	33.5(19)	66.6(14)	0.25(0)	120(42)	21(17)	1770(179)	47(48)	31(26)	193(8)	1098(116)	8.8(21)	35(29)	3.0(32)	16(18)	2.0(1)	1.3(0)	0.15(1)	0.014(0)	95(38)	0.025(0)	0.065	14(10)
Nanta Bula (n=11)	MIN	32.1	61.1	B.D.L.	19	B.D.L.	382	B.D.L.	B.D.L.	0.988	B.D.L.	1.9	0.13	B.D.L.	B.D.L.	B.D.L.	B.D.L.	B.D.L.	B.D.L.	2.9	B.D.L.	B.D.L.	3.8
	MAX	34.2	68.4	1.70	8919	20259	5984	4608	81	979	719	72	343	11	396	14	3.1	0.48	0.027	100	0.51	7.4	123
	GM	33.1	66.3	0.23	214	88	2041	78	0.25	1.9	95	2.9	1.06	0.49	-	8.1	0.15	1.0	0.067	3.7	0.049	5.5	8.70
	QR	33.4(11)	67.2(8)	0.3(0)	273(43)	1176(13)	4403(140)	201(40)	16(10)	75(18)	717(26)	11(1)	4(5)	4(5)	2.0(2)	2.0(2)	1.6(0)	0.048(1)	0.015(0)	38(12)	0.014(0)	0.78(0)	18(2)
Morococha (n=85)	MIN	31.8	64.6	B.D.L.	106	80	32	B.D.L.	38	22	11	4.7	0.41	0.17	0.04	B.D.L.	B.D.L.	B.D.L.	B.D.L.	0.8	0.0	0.11	-
	MAX	32.7	67.6	0.22	528	75	806	0.56	215	49	896	89	38	11	59	1.0	8.1	0.79	B.D.L.	69	0.34	1.1	-
	GM	32.3	68.2	0.042	283	37	309	0.43	87	58	6.6	5.7	12	2.9	1.8	3.6	1.7	0.20	0.24	-	25	0.17	2.2
	QR	33.3(12)	67.1(8)	0.05(0)	488(15)	66(3)	411(40)	0.60(29)	12(7)	81(36)	51(36)	75(28)	11(7)	3(10)	3(10)	5(10)	1(10)	0.15(0)	0.20(1)	-	19(28)	0.15(1)	0.24(1)
Morococha (n=85)	MIN	33.4	66.3	0.23	214	88	2041	78	0.25	1.9	95	2.9	1.06	0.49	-	8.1	0.15	1.0	0.067	3.7	0.049	5.5	8.70
	MAX	34.7	63.7	7.93	85.942	25.703	4727	111	1.14	2157	3427	24	307	6.7	4.0	13	1.2	0.0	0.058	21	0.067	0.66	70
	GM	33.2	64.3	1.36	11.066	1596	4052	82	0.34	34	323	5.9	18	0.39	0.098	1.9	1.1	0.77	0.055	6.3	0.063	0.042	28
	QR	33.5(10)	66.1(5)	2.7(0)	11.0(6)	1577(88)	3011(74)	4339(303)	166(1)	0.16(1)	64(2)	355(30)	8.8(5)	7.6(9)	1.6(1)	0.26(0)	2.9(1)	0.27(0)	3.2(1)	0.016(0)	7.6(4)	0.009(0)	0.025(0)
Morococha (n=85)	MIN	32.1	61.1	B.D.L.	19	B.D.L.	382	B.D.L.	B.D.L.	0.988	B.D.L.	1.9	0.13	B.D.L.	B.D.L.	B.D.L.	B.D.L.	B.D.L.	B.D.L.	2.9	B.D.L.	B.D.L.	3.8
	MAX	34.2	68.4	1.70	8919	20259	5984	4608	81	979	719	72	343	11	396	14	3.1	0.48	0.027	100	0.51	7.4	123
	GM	33.1	66.3	0.23	214	88	2041	78	0.25	1.9	95	2.9	1.06	0.49	-	8.1	0.15	1.0	0.067	3.7	0.049	5.5	8.70
	QR	33.4(11)	67.2(8)	0.3(0)	273(43)	1176(13)	4403(140)	201(40)	16(10)	75(18)	717(26)	11(1)	4(5)	4(5)	2.0(2)	2.0(2)	1.6(0)	0.048(1)	0.015(0)	38(12)	0.014(0)	0.78(0)	18(2)
Morococha (n=85)	MIN	31.8	64.6	B.D.L.	106	80	32	B.D.L.	38	22	11	4.7	0.41	0.17	0.04	B.D.L.	B.D.L.	B.D.L.	B.D.L.	0.8	0.0	0.11	-
	MAX	32.7	67.6	0.22	528	75	806	0.56	215	49	896	89	38	11	59	1.0	8.1	0.79	B.D.L.	69	0.34	1.1	-
	GM	32.3	68.2	0.042	283	37	309	0.43	87	58	6.6	5.7	12	2.9	1.8	3.6	1.7	0.20	0.24	-	25	0.17	2.2
	QR	33.3(12)	67.1(8)	0.05(0)	488(15)	66(3)	411(40)	0.60(29)	12(7)	81(36)	51(36)	75(28)	11(7)	3(10)	3(10)	5(10)	1(10)	0.15(0)	0.20(1)	-	19(28)	0.15(1)	0.24(1)
Morococha (n=85)	MIN	33.4	66.3	0.23	214	88	2041	78	0.25	1.9	95	2.9	1.06	0.49	-	8.1	0.15	1.0	0.067	3.7	0.049	5.5	8.70
	MAX	34.7	63.7	7.93	85.942	25.703	4727	111	1.14	2157	3427	24	307	6.7	4.0	13	1.2	0.0	0.058	21	0.067	0.66	70
	GM	33.2	64.3	1.36	11.066	1596	4052	82	0.34	34	323	5.9	18	0.39	0.098	1.9	1.1	0.77	0.055	6.3	0.063	0.042	28
	QR	33.5(10)	66.1(5)	2.7(0)	11.0(6)	1577(88)	3011(74)	4339(303)	166(1)	0.16(1)	64(2)	355(30)	8.8(5)	7.6(9)	1.6(1)	0.26(0)	2.9(1)	0.27(0)	3.2(1)	0.016(0)	7.6(4)	0.009(0)	0.025(0)
Morococha (n=85)	MIN	32.1	61.1	B.D.L.	19	B.D.L.	382	B.D.L.	B.D.L.	0.988	B.D.L.	1.9	0.13	B.D.L.	B.D.L.	B.D.L.	B.D.L.	B.D.L.	B.D.L.	2.9	B.D.L.	B.D.L.	3.8
	MAX	34.2	68.4	1.70	8919	20259	5984	4608	81	979	719	72	343	11	396	14	3.1	0.48	0.027	100	0.51	7.4	123
	GM	33.1	66.3	0.23	214	88	2041	78	0.25	1.9	95	2.9	1.06	0.49	-	8.1	0.15	1.0	0.067	3.7	0.04		

Table 4. Summary of element contents in galena from the Morococha district. Sulfur and Pb are given in wt% (EPMA data) and all trace elements, in ppm (LA-ICP-MS data).

Ore-body/vein	S (wt%)	Pb (wt%)	As (ppm)	Sb (ppm)	Fe (ppm)	Ag (ppm)	Cu (ppm)	Zn (ppm)	Se (ppm)	Mo (ppm)	Au (ppm)	Hg (ppm)	Tl (ppm)	Bi (ppm)	Cd (ppm)							
Entire district (n=44)	MIN	12.0	85.1	B.D.L.	B.D.L.	B.D.L.	272	32	B.D.L.	B.D.L.	0.090	B.D.L.	B.D.L.	0.98	B.D.L.	6.0						
	MAX	13.6	88.9	0.61	2.0	3.6	5712	5124	104	14	12	18	8.7	9.3	0.55	135						
	GM	13.1	87.4	0.091	0.53	0.056	1277	718	2.8	1.5	7.8	1.8	0.78	2.2	0.29	11	0.28	0.046	0.097	1.9	2.2	28
	IQR	13.2-13.0	88.1-86.9	0.28-0.043	1.2-0.33	0.064-0.043	1477-992	1069-346	9.3-0.57	1.6-1.1	8.5-7.1	2.1-1.2	3.2-0.20	3.6-1.0	0.32-0.27	92-1.4	0.35-0.22	0.048-0.032	0.087-0.077	2.1-1.5	199-0.028	34-24
Manto Italia (n=4)	MIN	-	-	0.33	B.D.L.	B.D.L.	4883	4326	B.D.L.	B.D.L.	3.0	-	6.7	B.D.L.	B.D.L.	B.D.L.	B.D.L.	3.8	0.022	26		
	MAX	13.5	84.8	0.39	B.D.L.	B.D.L.	5712	5124	B.D.L.	B.D.L.	12	7.4	-	8.1	B.D.L.	B.D.L.	B.D.L.	1.1	B.D.L.	3.9	0.031	36
	GM	-	-	0.35	-	-	5230	4663	-	-	8.1	5.2	-	7.5	-	-	-	0.090	-	3.8	0.027	31
	IQR	-	-	0.37-0.35	-	-	5442-4982	4855-4459	-	-	8.7-7.0	6.9-4.3	-	7.8-7.3	-	-	-	0.32-0.036	-	3.8-3.8	0.031-0.023	34-28
Morro Solar (n=3)	MIN	12.0	85.7	0.039	B.D.L.	B.D.L.	272	296	0.63	-	B.D.L.	-	0.25	B.D.L.	B.D.L.	B.D.L.	B.D.L.	0.040	0.38	1.2	81	6.0
	MAX	13.2	88.4	0.61	B.D.L.	B.D.L.	430	1157	104	-	B.D.L.	-	0.74	-	0.55	B.D.L.	B.D.L.	0.33	0.55	1.6	276	8.9
	GM	12.8	86.8	0.23	-	-	330	722	35	-	-	-	0.48	-	0.40	-	-	0.16	0.45	1.3	139	7.4
	IQR	13.2-12.9	88.4-86.4	0.56-0.28	-	-	360-290	1127-697	68-17	-	-	-	0.67-0.42	-	0.45-0.35	-	-	0.32-0.17	0.47-0.38	1.4-1.2	198-101	82-6.7
Ibette (n=17)	MIN	12.8	86.1	B.D.L.	B.D.L.	B.D.L.	480	32	B.D.L.	B.D.L.	B.D.L.	0.090	0.74	B.D.L.	29	B.D.L.	B.D.L.	B.D.L.	1.3	3.2	16	
	MAX	13.5	88.8	0.10	2.0	3.6	3449	1496	17	3.1	8.6	2.1	8.7	9.3	B.D.L.	135	0.67	0.14	0.889	4.5	6410	68
	GM	13.1	87.4	0.093	1.1	0.068	1171	318	2.2	1.4	7.8	1.3	1.2	1.8	-	81	0.28	0.045	0.076	2.0	309	29
	IQR	13.2-13.0	88.2-86.9	0.074-0.039	1.5-0.89	0.068-0.046	1433-981	475-219	9.8-0.43	1.7-0.93	8.5-7.1	1.4-1.1	4.1-0.14	2.5-1.0	-	108-63	0.37-0.22	0.052-0.033	0.085-0.070	2.2-1.7	1800-42	82-6.7
Rosita/Rubi (n=20)	MIN	12.5	85.1	B.D.L.	B.D.L.	B.D.L.	937	797	B.D.L.	B.D.L.	B.D.L.	0.02	0.52	B.D.L.	B.D.L.	B.D.L.	B.D.L.	B.D.L.	0.88	B.D.L.	24	
	MAX	13.6	88.9	B.D.L.	0.46	0.052	1983	1571	15	14	B.D.L.	18	4.5	5.8	B.D.L.	20	B.D.L.	0.046	1.3	2.4	6.18	41
	GM	13.1	87.5	-	0.33	0.045	1270	988	3.9	1.7	-	1.9	0.58	2.3	-	3.7	-	0.034	0.10	1.6	0.041	31
	IQR	13.3-13.0	88.1-87.2	-	0.34-0.32	0.052-0.038	1352-1033	1056-803	6.3-3.2	2.9-1.1	-	2.4-1.2	2.9-0.30	3.5-1.5	-	20-1.3	-	0.039-0.029	0.065-0.070	2.1-1.2	0.095-0.035	33-30

G.M.: Geometric means of element content. B.D.L.: below detection limit. EPMA data in wt%. LA-ICP-MS data in ppm.

G.M.: Geometric means of element content. B.D.L.: below detection limit. EPMA data in wt%. LA-ICP-MS data in ppm.

Table 5. Summary of element contents in tetrahedrite-group minerals from the Morococha district. Sulfur, Cu, Fe, Sb, As, and Ag are given in wt% (EPMA data) and all trace elements, in ppm (LA-ICP-MS data).

Ore-body/vein	S (wt%)	As (wt%)	Sb (wt%)	Fe (wt%)	Ag (wt%)	Cu (wt%)	Zn (wt%)	In (ppm)	Ge (ppm)	Ga (ppm)	Sn (ppm)	Pb (ppm)	Mn (ppm)	Co (ppm)	Se (ppm)	Mo (ppm)	Au (ppm)	Hg (ppm)	Tl (ppm)	Bi (ppm)	Cd (ppm)	
Entire district (n=12)	MIN	24.0	3.33	B.D.L.	0.13	B.D.L.	25.9	2.05	0.39	B.D.L.	B.D.L.	B.D.L.	1.1	B.D.L.	B.D.L.	B.D.L.	B.D.L.	62	B.D.L.	B.D.L.	653	
	MAX	29.0	22.8	24.7	5.92	17.5	44.1	9.15	266	3.3	9.6	24	15	4008	2.0	152	3.2	446	0.88	66,892	1907	
	GM	27.2	12.0	5.54	0.58	0.86	40.1	6.99	23	1.2	1.5	1.8	4.2	596	0.36	23	0.70	0.16	147	0.11	359	1236
	IQR	28.3-26.2	21.3-7.54	19.3-0.68	0.99-0.33	1.46-0.18	42.3-39.2	8.12-6.68	44-25	1.9-0.78	3.8-0.65	12-0.42	7.2-2.7	3610-587	0.62-0.27	68-14	0.91-0.34	0.51-0.143	196-94	0.22-0.067	18,786-24	1627-104
Epithermal overprint on Toconacho porphyry (n=4)	MIN	27.8	15.0	1.65	0.13	B.D.L.	42.3	6.43	30	0.64	3.3	B.D.L.	1.1	371	0.22	64	0.29	B.D.L.	169	0.041	17,447	982
	MAX	28.0	18.1	5.36	0.28	B.D.L.	44.1	9.15	48	1.3	9.6	0.85	8.0	462	0.32	152	0.34	0.046	212	0.087	66,892	1136
	GM	27.9	16.5	2.70	0.22	-	43.2	7.39	38	0.89	5.3	0.29	2.9	409	0.28	103	0.32	0.027	188	0.058	36,518	1068
	IQR	27.9-27.9	17.5-15.5	2.78-2.11	0.25-0.25	-	44.0-43.8	7.30-7.10	44-33	1.3-0.65	7.3-3.7	0.43-0.23	6.8-1.2	438-387	0.30-0.27	148-76	0.34-0.30	0.039-0.020	196-180	0.070-0.046	66,842-21,464	1102-104
Morro Solar (n=2)	MIN	25.0	3.56	B.D.L.	0.16	0.17	37.8	6.72	229	0.77	0.31	30	-	B.D.L.	B.D.L.	19	0.67	1.9	402	-	3.9	653
	MAX	29.0	22.8	24.7	0.87	1.48	42.3	8.37	266	3.3	0.36	17	-	60	B.D.L.	20	1.3	3.2	446	-	31	796
	GM	27.5	13.3	3.60	0.41	0.50	40.5	7.91	247	1.6	0.33	13	-	11	-	19	0.94	2.5	424	-	11	721
	IQR	28.8-26.2	22.0-6.65	20.6-0.14	0.55-0.33	1.15-0.22	41.9-39.5	8.25-7.73	257-239	2.7-1.4	0.35-0.32	15-12	-	45-16	-	20-19	1.1-0.83	2.9-2.2	435-413	-	24-11	761-489
Ibette (n=4)	MIN	26.1	7.37	B.D.L.	0.63	0.06	38.1	2.05	23	B.D.L.	3.1	1.0	4.2	3529	B.D.L.	13	B.D.L.	B.D.L.	62	B.D.L.	1102	1614
	MAX	28.7	21.8	19.4	5.92	2.26	43.1	7.57	27	1.8	3.9	24	15	4008	B.D.L.	18	3.2	B.D.L.	102	0.17	1379	1907
	GM	27.3	13.2	9.23	1.39	0.91	41.0	5.82	26	1.6	3.5	4.7	8.8	3806	-	15	1.4	-	85	0.12	1225	1691
	IQR	28.3-26.4	20.5-10.1	15.9-1.10	1.89-1.01	1.79-0.86	42.9-39.9	6.94-6.01	26-25	1.9-1.6	3.8-3.4	20-1.1	9.3-5.1	3892-3771	-	16-14	2.7-0.75	-	97-81	0.18-0.079	1325-1127	1705-162
Rosita/Rubi (n=2)	MIN	24.0	3.13	23.8	0.45	2.78	25.9	5.63	0.39	B.D.L.	0.46	-	1453	B.D.L.	B.D.L.	B.D.L.	0.40	80	0.28	B.D.L.	1318	
	MAX	25.4	3.68	24.2	2.37	17.5	37.1	6.95	1.0	2.1	B.D.L.	5.9	-	2088	B.D.L.	B.D.L.	B.D.L.	0.75	103	0.48	0.27	1734
	GM	24.8	3.42	24.0	0.84	7.2	31.7	6.42	0.63	1.1	-	1.7	-	1742	-	-	-	0.55	91	0.37	0.098	1512
	IQR	25.3-24.5	3.57-3.30	24.3-23.9	1.46-0.50	12.65-5.31	35.2-29.6	6.86-6.20	0.84-0.54	1.7-0.99	-	4.6-1.8	-	1929-1612	-	-	-	0.66-0.49	97-86	0.43-0.33	0.21-0.094	1630-142

G.M.: Geometric means of element content. B.D.L.: below detection limit. EPMA data in wt%. LA-ICP-MS data in ppm.

G.M.: Geometric means of element content. B.D.L.: below detection limit. EPMA data in wt%. LA-ICP-MS data in ppm.

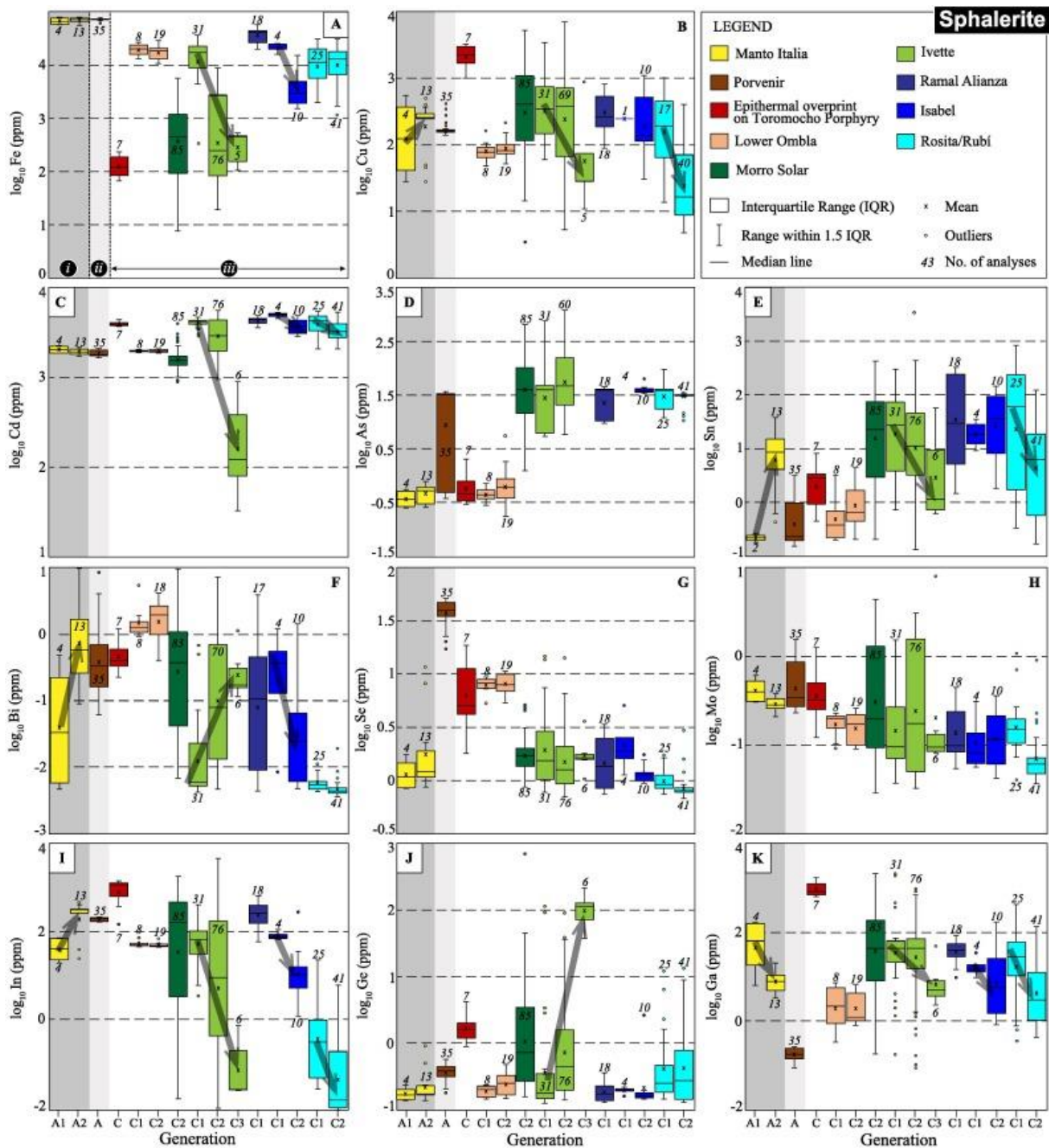


Fig. 9. Selected boxplots of log-transformed element contents in sphalerite (LA-ICP-MS data). Dark gray arrows indicate temporal trends within sites during a same [mineralization](#) event. “i” (Manto Italia), “ii” (Porvenir), and “iii” (other sites) refer to the mineralization events described in [Section 2.3](#) (“Studied polymetallic mineralization styles in the Morococha district”). The ordering of the boxplots in “iii” follows a roughly proximal to distal position relative to the Toromocho porphyry. Analyzed sphalerite from Manto Italia and Porvenir comes from LS assemblages, that from veins overprinting the Toromocho porphyry from HS assemblages; whereas for the other sites, sphalerite comes from IS assemblages. Zinc tends to show a negative correlation with Fe ([Fig. 10A](#)) suggesting simple $Fe^{2+} \leftrightarrow Zn^{2+}$ substitution, at least at $Fe > \sim 1$ wt% ([Cook et al., 2009](#), [Lockington et al., 2014](#), [Wei et al., 2018](#), [Pring et al., 2020](#)). In contrast, Zn and Cd do not show correlation. A positive correlation between Fe and Mn ([Fig. 10B](#)) suggests either additional $Fe^{2+} + Mn^{2+} \leftrightarrow 2Zn^{2+}$ substitution ([Graeser, 1969](#), [Cook et al., 2009](#), [Pring et al., 2020](#)) or similar controls acting on the concentration of these elements (e.g., temperature: [Frenzel et al., 2016](#)). This relationship diverges from the negative correlation between both elements observed by [Di Benedetto et al. \(2005\)](#). Dispersion, however, points to more complex Zn substitution mechanisms involving trace elements, as explained below.

Sphalerite

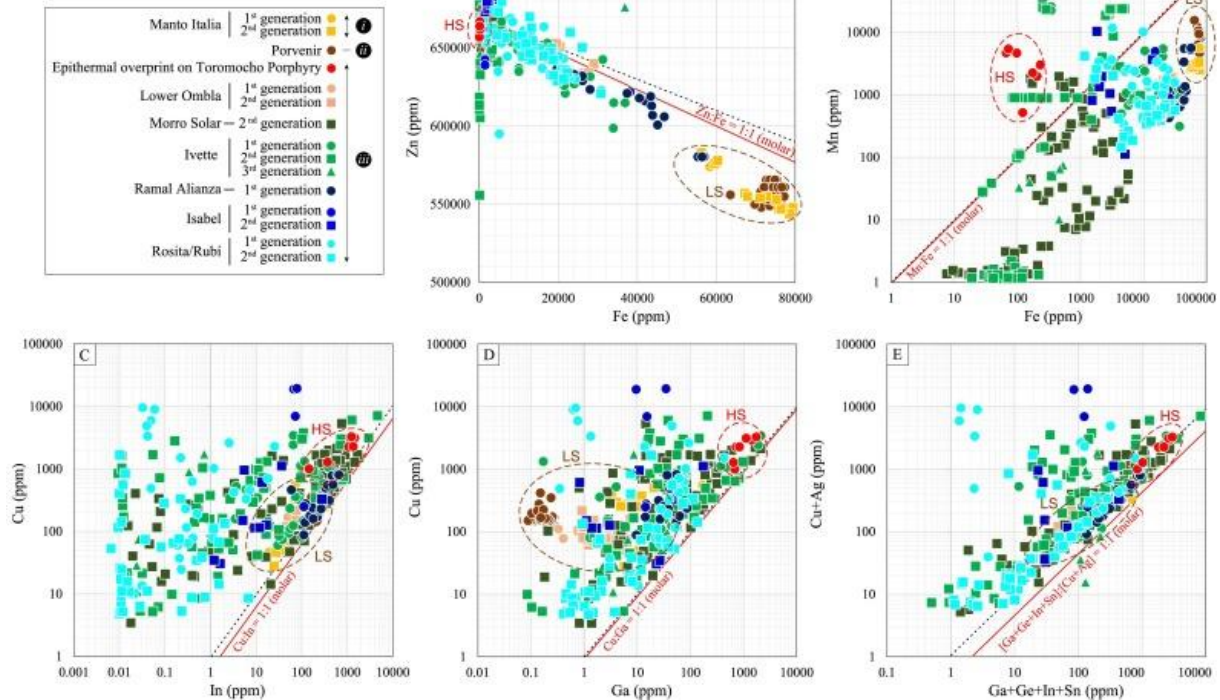


Fig. 10. Correlation between elements in sphalerite from the Morococha district. Black dashed lines indicate ppm ratios and red lines, molar ratios. “i”, “ii”, and “iii” refer to the [mineralization](#) events described in [Section 2.3](#) (Studied polymetallic mineralization styles in the Morococha district). Compositional fields for studied sphalerite from *skarn* bodies are highlighted. Compositional fields for sphalerite in HS (high-sulfidation; epithermal veins overprinting the Toromocho stock) and LS (low-sulfidation; Manto Italia and Porvenir) assemblages are highlighted. The rest of the data correspond to sphalerite from intermediate-sulfidation assemblages.

Copper values are generally higher in sphalerite grains from high-sulfidation assemblages overprinting the Toromocho porphyry (3009–1771 ppm Cu) and some intermediate-sulfidation assemblages including Ivette (730–89 ppm Cu), Morro Solar (1099–116 ppm Cu), and Ramal Alianza (536–188 ppm Cu; [Fig. 9B](#)). Higher Cd contents ([Fig. 9C](#)) are reported in sphalerite grains from intermediate-sulfidation assemblages in Ivette (1st- and 2nd-generation; 4355–2442 ppm), Ramal Alianza (4541–4034 ppm), Isabel (4804–3381 ppm), and Rosita/Rubi (4296–2854 ppm), and in grains from high-sulfidation assemblages overprinting the Toromocho porphyry (4012–3710 ppm). There is a general trend to Cd depletion from early to late sphalerite generations in intermediate-sulfidation assemblages, particularly in Ivette (3rd-generation, 431–80 ppm; [Fig. 9C](#)). The As content increases notably in sphalerite from intermediate-sulfidation assemblages, especially in Morro Solar (103–15 ppm) and Ivette (122–19 ppm), relative to sphalerite from high- (0.79–0.33 ppm) and low-sulfidation (e.g., Manto Italia, 0.61–0.30 ppm) assemblages ([Fig. 9D](#)). Tin contents are markedly variable in different mineralization style and sphalerite generation ([Fig. 9E](#)). Tin content is, in general, lower in grains from high-sulfidation (3.4–1.1 ppm) and low-sulfidation (e.g., Porvenir, 0.98–0.19 ppm) assemblages. Except for Lower Ombla (1.2–0.41 ppm), Sn contents are significantly higher in intermediate-sulfidation sphalerite grains from Ivette (47–3.0 ppm), and Morro Solar, Ramal Alianza, Isabel, and Rosita/Rubi (75–2.0 ppm). In low-sulfidation assemblages from Manto Italia, there is a marked Sn enrichment from first- (0.24–0.20 ppm) to second-generation (15–4.1 ppm) sphalerite. In intermediate-sulfidation assemblages, in contrast, there is a trend towards Sn depletion from early to late sphalerite generations. Bismuth contents in sphalerite are systematically low (<10 ppm) with subtle depletion in distal (e.g., Rosita/Rubi, 0.0056–0.0043 ppm) relative to proximal (e.g., Lower Ombla, 2.3–1.0 ppm) intermediate-sulfidation assemblages ([Fig. 9F](#)). Bismuth shows both enrichment and depletion trends from early to late sphalerite generations. Selenium content is also generally low. The highest Se contents are recorded in low-sulfidation assemblages from Porvenir (48–35 ppm). In sphalerite from intermediate-sulfidation assemblages (2.1–0.90 ppm), there is Se depletion from proximal to distal mineralized structures ([Fig. 9G](#)). Cobalt is distinctly enriched in sphalerite from Porvenir (280–171 ppm), whereas in the rest of the studied structures, Co is typically below 10 ppm. Molybdenum content in the studied sphalerite generations is systematically low (0.36–0.079 ppm) with a slight, steady decrease from high-sulfidation (0.50–0.25 ppm) to distal intermediate-sulfidation (e.g., Rosita/Rubi, 0.17–0.055 ppm; [Fig. 9H](#)) mineralization.

The In content in sphalerite is much higher in high-sulfidation assemblages in epithermal veins overprinting the Toromocho porphyry mineralization (1291–726 ppm, up to 1456 ppm) than in the other analyzed sphalerite. In low-sulfidation assemblages, In content is also relatively high (e.g., Porvenir, 209–171 ppm); in Manto Italia, the In content increases from first- (68–23 ppm) to second-generation (324–261 ppm) sphalerite. In intermediate-sulfidation assemblages, sphalerite is particularly enriched in In in Morro Solar (471–8.0 ppm, up to 1804 ppm) and Ramal Alianza (398–157 ppm, up to 657 ppm; [Fig. 9I](#)); the In content tends to decrease towards the more distal mineralization at Isabel and Rosita/Rubi (5.3–0.089 ppm). In contrast to sphalerite from Manto Italia, in sphalerite from intermediate-sulfidation assemblages there is a dramatic In depletion from early to late generations.

[Germanium](#) values are generally low (0.89–0.18 ppm) and only third-generation, colloform sphalerite grains from Ivette exhibit significantly higher values (129–74 ppm Ge; [Fig. 9J](#)). [Gallium](#) contents ([Fig. 9K](#)) are much higher in sphalerite from

high-sulfidation assemblages (1269–706 ppm) and significant in grains from intermediate-sulfidation assemblages in Morro Solar (191–8.0 ppm, up to 2118 ppm). There is a subtle but systematic decrease in the Ga content from early to late sphalerite generations in both low- and intermediate-sulfidation assemblages. Correlations and substitution mechanisms for In, Ge, and Ga in sphalerite are addressed in detail in the Discussion section.

5.2. Chalcopyrite

Tin content in chalcopyrite increases by two orders of magnitude from Lower Ombla (25–14 ppm) to the distal Ramal Alianza (1115–585 ppm; Fig. 11A). Silver in chalcopyrite also displays relatively high (143–14 ppm), though erratic, values at the district scale (Fig. 11B). The highest Ag content is found in low-sulfidation assemblages in Manto Italia (2187–1722 ppm), followed by intermediate-sulfidation assemblages in Lower Ombla (with higher values in the first [228–215 ppm] than in the third [30–13 ppm] generations). The lowest Ag content is found in chalcopyrite grains from the high-sulfidation assemblages overprinting the Toromocho porphyry (1.2–0.39 ppm). Selenium content is high in chalcopyrite from Lower Ombla, particularly in grains of the first generation (111–109 ppm; Fig. 11C), relative to those of the third generation (18–17 ppm), and progressively decreases towards distal mineralization (e.g., Ramal Alianza, 4.2–3.1 ppm). Mercury content is high in chalcopyrite from Lower Ombla, particularly in grains of the first generation (1.2–0.39 ppm), relative to those of the third generation (18–17 ppm), and progressively decreases towards distal mineralization (e.g., Ramal Alianza, 4.2–3.1 ppm). Mercury shows low values and progressive depletion from high-sulfidation epithermal overprint in the Toromocho porphyry center (0.30–0.17 ppm) to the more distal intermediate-sulfidation mineralization (e.g., Ramal Alianza, <0.13 ppm; Fig. 11D).

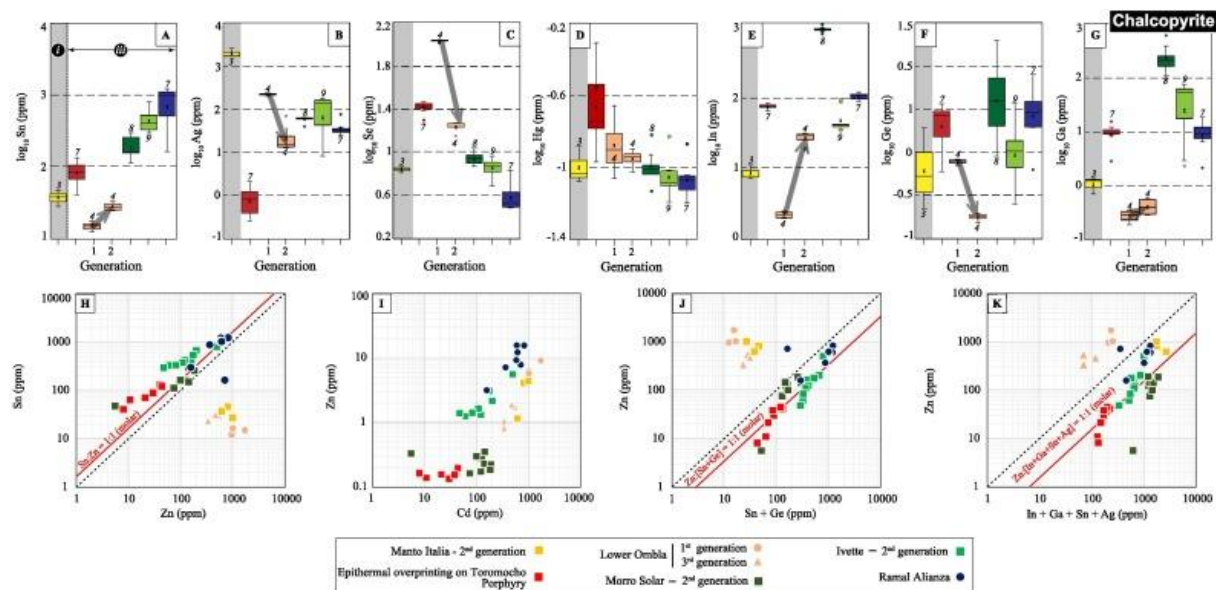


Fig. 11. Selected boxplots of log-transformed element contents (A-G) and correlation between elements (H-K) in chalcopyrite from the Morococha district. In boxplots, legend is as in Fig. 9, dark gray arrows indicate temporal trends within sites, and “i” (Manto Italia) and “iii” (other sites) refer to the mineralization events described in Section 2.3 (“Studied polymetallic mineralization styles in the Morococha district”). The ordering of the boxplots in “iii” follows a roughly proximal to distal position relative to the Toromocho porphyry. In correlation diagrams, black dashed lines indicate ppm ratios and red lines, molar ratios.

A positive correlation between the Zn and Sn content in chalcopyrite is observed (Fig. 11H), although grains from Lower Ombla and Manto Italia seem to deviate from this trend. Noteworthy, Sn contents in chalcopyrite (360–42 ppm) are significantly higher than in sphalerite (47–0.81 ppm). Zinc also correlates positively with Cd (Fig. 11I; see George et al., 2018, Wilson, 2019).

Indium contents are erratic throughout the Morococha chalcopyrite database. Distinctively high In values are recorded in chalcopyrite from intermediate-sulfidation assemblages in Morro Solar (941–891 ppm) and Ramal Alianza (113–93 ppm), followed by chalcopyrite from high-sulfidation assemblages in the Toromocho porphyry center (77–71 ppm). In Lower Ombla, there is a marked increase in the In content from the first (2.3–1.9 ppm) to the third (30–25 ppm) generations of chalcopyrite (Fig. 11E). Germanium contents are systematically low (3.1–0.68 ppm) and show depletion from the first (0.81–0.75 ppm) to the third (0.19–0.17 ppm) generations in Lower Ombla (Fig. 11F). The highest Ga content in chalcopyrite occurs in intermediate-sulfidation assemblages in Morro Solar (295–160 ppm; Fig. 11G).

5.3. Galena

The highest Ag content in galena occurs in low-sulfidation assemblages in Manto Italia (5442–4982 ppm) and, to a lesser extent, in intermediate-sulfidation assemblages in Ivette (1433–981 ppm) and Rosita/Rubí (1352–1033 ppm; Table 4, Fig. 12A). Galena from Morro Solar contains the lowest Ag (369–290 ppm). Silver displays fair positive correlations with Bi and Sb (Fig. 12E-G) that agree with widely described coupled substitutions (e.g., Foord et al., 1988, Sack, 2005, Sack and Ebel, 2006, Sack and Goodell, 2002, Sack and Lichtner, 2009). In Ivette, element correlations suggest coupled substitution of the type $\text{Bi}^{3+} + \text{Ag}^+ \leftrightarrow 2\text{Pb}^{2+}$ (Fig. 12E-F; Armbruster et al., 2003, Renock and Becker, 2011, George, 2013, George et al., 2015).

In Manto Italia and Rosita/Rubí, the strong positive correlation of Ag + Cu + Tl and Bi + Sb (Fig. 12G) suggests (Ag, Cu, Tl)⁺ + (Bi, Sb)³⁺ ↔ 2Pb²⁺ coupled substitution, as proposed by George et al. (2015).

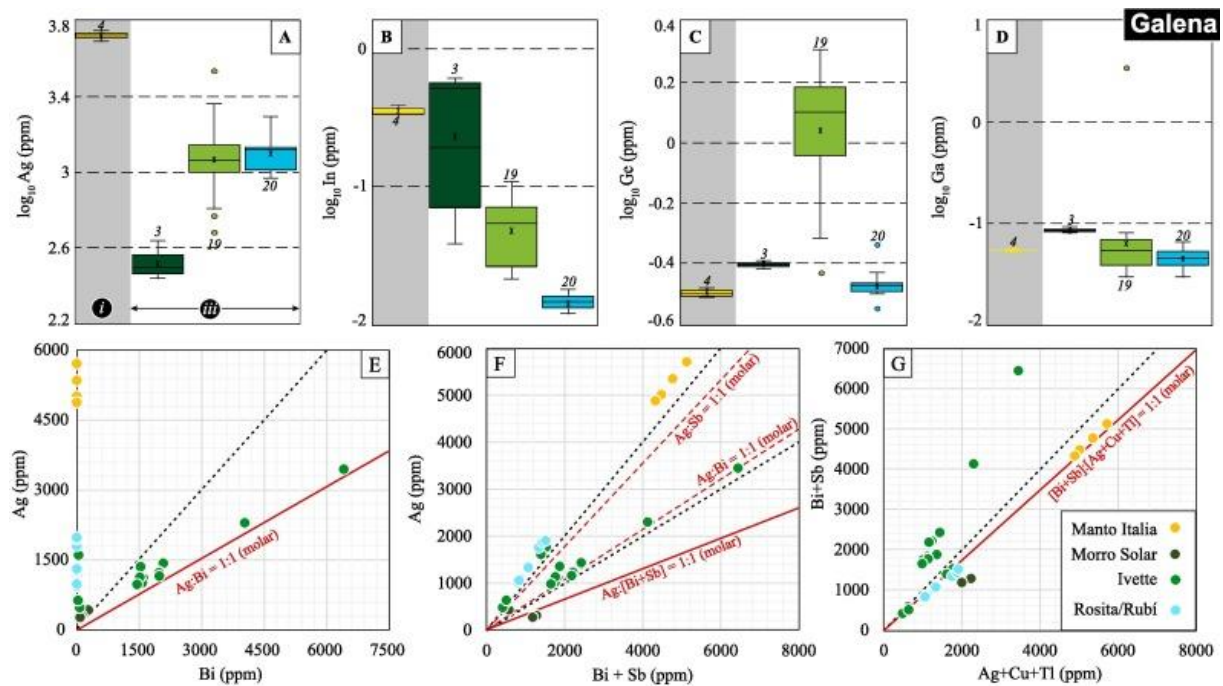


Fig. 12. Selected boxplots of log-transformed element contents (A-D) and correlation between elements (E-G) in galena from the Morococha district. In boxplots, legend is as in Fig. 9, and “i” (Manto Italia) and “iii” (other sites) refer to the mineralization events described in Section 2.3 (“Studied polymetallic mineralization styles in the Morococha district”). The ordering of the boxplots in “iii” follows a roughly proximal to distal position relative to the Toromocho porphyry. In correlation diagrams, black dashed lines indicate ppm ratios and red lines, molar ratios. The In, Ge, and Ga contents in galena from Morococha yield values <3.6 ppm (Fig. 12B-D). In intermediate-sulfidation assemblages, the In content is highest in galena from Morro Solar (0.56–0.28 ppm) and displays a progressive depletion from proximal to distal mineralization.

5.4. Tetrahedrite-tennantite series minerals

Copper content in tetrahedrite-tennantite series minerals tends to decrease from grains in epithermal veins overprinting the Toromocho porphyry mineralization (44.0–43.0 wt%) to distal mineralization (Rosita-Rubí, 35.2–29.6 wt%; Fig. 13A), following an opposite trend to Ag (with the highest values in distal Rosita-Rubí, 12.7–5.3 wt%; Fig. 13B; Table 5) due to the substitution between both elements in the crystal lattice. The Fe and Zn contents show more irregular patterns (Fig. 13C-D). Analyzed grains correspond to tetrahedrite and tennantite, with respective average empirical formulas $(\text{Cu}_{8.93}\text{Ag}_{0.80})(\text{Zn}_{1.70}\text{Fe}_{0.23})(\text{Sb}_{2.87}\text{As}_{1.13})\text{S}_{12.66}$ and $(\text{Cu}_{9.61}\text{Ag}_{0.08})(\text{Zn}_{1.51}\text{Fe}_{0.33})(\text{As}_{3.52}\text{Sb}_{0.48})\text{S}_{12.68}$. Tetrahedrite-tennantite series minerals from Ramal Alianza and epithermal veins overprinting the Toromocho porphyry classify as tennantite, grains from Morro Solar and Ivette, as both tennantite and tetrahedrite, and grains from Rosita/Rubí, as tetrahedrite.

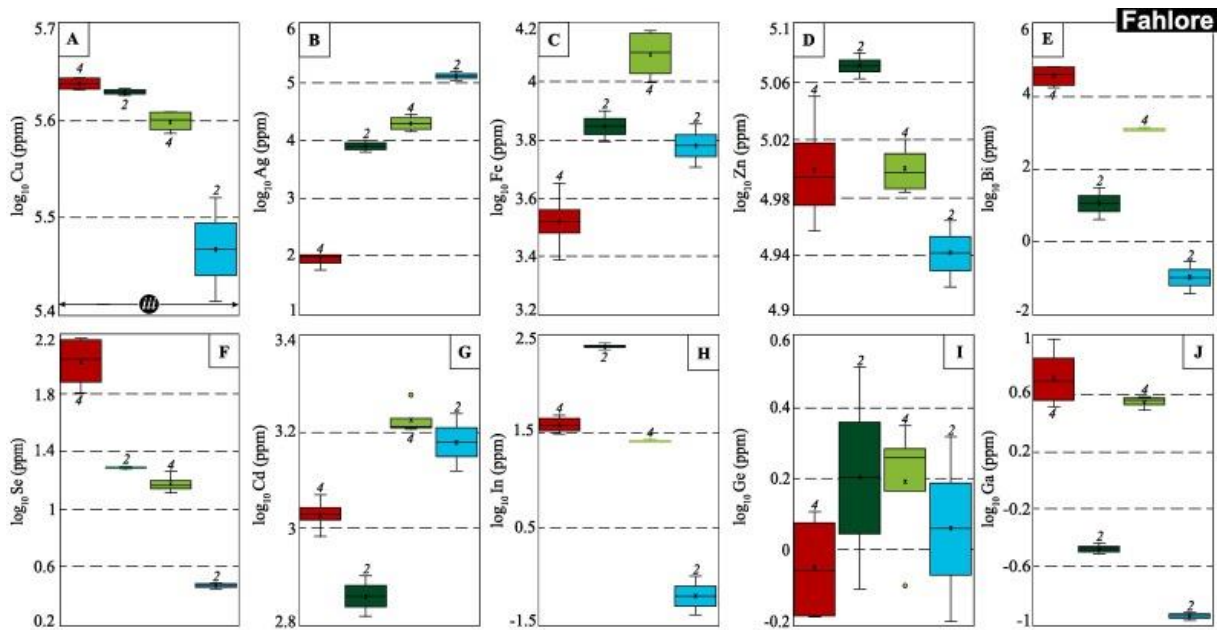


Fig. 13. Selected boxplots of log-transformed element contents in tetrahedrite-tennantite series minerals. Legend as in Fig. 9. “iii” refers to the last mineralization event described in Section 2.3 (“Studied polymetallic mineralization styles in the Morococha district”). The ordering of the boxplots follows a roughly proximal to distal position relative to the Toromocho porphyry.

Tennantite from epithermal veins overprinting the Toromocho porphyry contains the highest Bi content (66842–21464 ppm), which tends to decrease in more distal mineralization (Rosita/Rubí, 0.21–0.094 ppm; Fig. 13E). Selenium shows a similar distribution as Bi, with the highest values recorded in grains from epithermal veins overprinting the Toromocho porphyry mineralization (148–76 ppm) and showing a sustained decrease towards distal mineralization (Fig. 13F). In contrast, the highest Cd contents are found in Ivette and Rosita/Rubí (1709–1616 ppm; Fig. 13G) and the lowest, in Morro Solar (761–689 ppm).

The highest In contents in tetrahedrite-tennantite occur in Morro Solar (257–239 ppm) followed by tetrahedrite-tennantite in epithermal veins from the Toromocho porphyry center (44–33 ppm) and Ivette (26–25 ppm; Fig. 13H). The In content in tetrahedrite-tennantite from Rosita/Rubí is mostly below detection limits. The Ge (1.9–0.74 ppm) and Ga (3.8–0.65 ppm) contents are low and do not show clear trends at the district scale (Fig. 13I–J).

6. Discussion

6.1. Geochemical behavior of In, Ge, and Ga

The studied mineralized structures in the Morococha district do not host independent In, Ge and Ga minerals, but these elements are systematically found in trace amounts in the analyzed minerals (sphalerite, chalcopyrite, galena, and tetrahedrite-tennantite) yet with contrasting values. Indium is more abundant in sphalerite (217–2.7 ppm, up to 4608 ppm) and in chalcopyrite (109–32 ppm, up to 1070 ppm), whereas its content is low in tetrahedrite-tennantite (44–25 ppm, up to 266 ppm) and galena (0.28–0.043 ppm, up to 0.61 ppm). In coeval generations of sphalerite and chalcopyrite, the average In content is at least two times higher in sphalerite than in chalcopyrite (e.g., Ramal Alianza, 398–157 ppm in sphalerite, 113–93 ppm in chalcopyrite). Indium partitioning into sphalerite, and resulting elevated content, are widely documented (Cook et al., 2009, Cook et al., 2011a, Cook et al., 2011b, Sahlström et al., 2017, Bauer et al., 2019a, Frenzel et al., 2019, Torró et al., 2019a, Torró et al., 2019b). At Morococha, Ga also concentrates in sphalerite (61–2.0 ppm, up to 2137 ppm) and chalcopyrite (62–1.5 ppm, up to 630 ppm), and is far lower in tetrahedrite-tennantite (3.8–0.65 ppm, up to 9.6 ppm) and galena (mostly below detection limits, up to 3.6 ppm). The Ge content is systematically very low in all the analyzed minerals (1.2–0.2.0 ppm), except some anomalously high values locally found in late sphalerite (3rd generation in the Ivette Manto, 129–74 ppm). Sphalerite is volumetrically the most abundant component in the studied polymetallic mineralization at Morococha and therefore represents the main host for In and Ga at the district scale. It is noteworthy that sphalerite from the giant Cerro de Pasco Cordilleran deposit in Peru (Rottier et al., 2018) yields broadly equivalent ranges for In (165–17 ppm, up to 1449 ppm), Ga (58–1.7 ppm, up to 423 ppm), and Ge (4.3–3.5 ppm, up to 71 ppm) contents thus suggesting that the presented Morococha sphalerite dataset (Table 2) is likely to be representative of sphalerite compositions in Cordilleran type mineralization in terms of these three elements.

The In and Cu values in the studied sphalerite plot mostly at In:Cu (molar) of 1:1 (Fig. 10C) pointing to a $\text{Cu}^+ + \text{In}^{3+} \leftrightarrow 2\text{Zn}^{2+}$ coupled substitution. This substitution has been previously identified as the dominant one for the incorporation of In in sphalerite (e.g., Schwarz-Schampera and Herzig, 2002, Cook et al., 2012, Torró et al., 2019a) and conforms to the solid solution between sphalerite and roquesite [CuInS₂] (Parasyuk et al., 2003, Schorr and Wagner, 2005) within the sphalerite – stannite – roquesite pseudoternary system described by Oen et al. (1980). However, there is a set of sphalerite data, which includes part of Ivette, Morro Solar, Isabel, and Rosita/Rubí analyses, that lies above the correlation line in Fig. 10C, thus denoting higher Cu at a given In content. A similar situation is noticed by other authors such as Xu et al. (2020) and points to the existence of other coupled substitutions involving Cu, as it is further discussed below.

A positive correlation between Ga and Cu in sphalerite (Fig. 10D) suggests a $\text{Cu}^+ + \text{Ga}^{3+} \leftrightarrow 2\text{Zn}^{2+}$ coupled substitution (see Johan, 1988, Murakami and Ishihara, 2013, Bonnet et al., 2016, Pring et al., 2020). The distributions of Cu, In, and Ga (Fig. 10 C-D) would indicate that these two substitutions might have operated independently. An additional $(\text{Sn}, \text{Ge})^{4+} + (\text{Ga}, \text{In})^{3+} + (\text{Cu}, \text{Ag})^+ \leftrightarrow 4\text{Zn}^{2+}$ coupled substitution (see Cook et al., 2009) cannot be ruled out either (Fig. 10E), particularly in grains from Porvenir, Manto Italia, and Lower Ombla. According to these observations, the incorporation of In and Ga within the crystal lattice of sphalerite might have involved different substitution schemes in which Cu was always present.

It is noteworthy, however, that the incorporation of In in the sphalerite crystal lattice is decoupled from Fe based on the lack of correlation between the two elements. For instance, the highest In content, recorded in sphalerite from high-sulfidation epithermal veins in the Toromocho porphyry center, occur in Fe-poor sphalerite (189–85 ppm Fe).

Regarding chalcopyrite analyses, there is a positive correlation of both Sn + Ge and In + Ga + Sn + Ag with Zn in grains from the epithermal veins overprinting the Toromocho porphyry mineralization and intermediate-sulfidation assemblages at Ivette, Morro Solar, and Ramal Alianza (Fig. 11J-K). However, since chalcopyrite is not fully ionic, formulating substitutions requires caution. Several authors, including Todd et al., 2003, Mikhlin et al., 2005, Pearce et al., 2006, Klekovkina et al., 2014, proposed two different valence states for Cu and Fe in chalcopyrite [$\text{Cu}^{2+}\text{Fe}^{2+}\text{S}_2$ vs. $\text{Cu}^+\text{Fe}^{3+}\text{S}_2$]. However, other authors (e.g., Li et al., 2013) suggest intermediate valence states. Thus, the incorporation of trace elements within the chalcopyrite lattice is not fully constrained yet. Silver is one of the most widely reported elements that can be incorporated within the chalcopyrite crystal lattice (George et al., 2018), while In, Ga, and Ge can also be incorporated to a lesser extent. Due to the relative good correlation observed between these elements and Zn and Sn (Fig. 11J-K), we suggest that Ag may be introduced in coupled substitutions involving $\text{Cu}^{(+)}$, $\text{Ag}^{(+)}$, $\text{Zn}^{(2+)}$, $\text{In}^{(3+)}$, $\text{Ga}^{(3+)}$, $\text{Sn}^{(4+)}$ and, $\text{Ge}^{(2+/4+)}$, as proposed by Belissant et al., 2019, Reich et al., 2020.

The systematically very low In, Ge, and Ga contents in galena and tetrahedrite-tennantite grains from the Morococha district preclude any possible identification of incorporation mechanisms based upon the correlations between element contents.

6.2. Sphalerite geothermometry: testing the GGIMFis geothermometer in the Morococha district

Oftedal, 1940, Warren and Thompson, 1945 pioneered the idea that crystallization temperature is closely related to the composition of sphalerite in terms of its minor and trace-elements composition. Wei et al. (2018) suggested that high contents of Fe, Mn, and In, and low contents of Ga and Ge in sphalerite relate to high-temperature deposits. Frenzel et al. (2016) further developed the idea that the composition of sphalerite depends on its crystallization temperature but also on the mineralization style, and by using fluid inclusion microthermometric data established a correlation between the crystallization temperature and sphalerite composition in terms of Ga, Ge, In, Mn, and Fe, referred to as the GGIMFis geothermometer.

The GGIMFis geothermometer has been applied to sphalerite analyzed here (Table 6; Fig. 14) yielding temperatures ranging from approx. 400 °C to below 100 °C. The highest GGIMFis temperatures are recorded in near skarn mineralization including both Stage A (Porvenir: 407 ± 8 °C, 2-sigma error °C; Manto Italia: 334 ± 23 °C in slA1, and 359 ± 24 °C in slA2) and Stage C (Lower Ombla: 358 ± 26 °C in slC1, and 328 ± 25 °C in slC2) sphalerite grains. In contrast, Stage C sphalerite grains from high-sulfidation assemblages in Cordilleran veins overprinting the Toromocho porphyry yield a much lower GGIMFis temperature of 157 ± 33 °C. Stage C sphalerite grains from Cordilleran intermediate-sulfidation assemblages yield GGIMFis temperatures in the range between $323 \pm 39^\circ$ and 81 ± 26 °C, with a general decrease in the crystallization temperatures from early to late generations (e.g., in Ivette, slC1, slC2, and slC3 yield GGIMFis temperatures of $285 \pm 81^\circ$, $173 \pm 194^\circ$ and 81 ± 26 °C, respectively) and from porphyry-proximal to porphyry-distal position (Table 6).

Table 6. Formation temperature of sphalerite according to the GGIMFis geothermometer of Frenzel et al. (2016).

Paragenesis	Site	Generation	N	Mean	Abs error*	1-sigma**	2-sigma
Stage A (low sulfidation)	Porvenir	slA	35	407	28	4	8
	Manto Italia	slA1	4	334	26	12	23
		slA2	13	359	32	12	24
Stage C (high sulfidation)	Epithermal overprint on Toromocho Porphyry	slC	7	157	29	17	33
Stage C (intermediate sulfidation)	Lower Ombla	slC1	8	335	32	13	26
		slC2	19	328	32	12	25
	Morro Solar	slC2	85	154	142	61	122
	Ivette	slC1	31	285	56	40	81
		slC2	76	173	142	97	194
		slC3	5	81	45	13	26
	Ramal Alianza	slC1	18	323	39	19	39
	Isabel	slC1	4	310	20	13	26
		slC2	10	288	147	52	105
	Rosita/Rubí	slC1	25	263	57	29	58
slC2		41	254	60	34	69	

*Relative to the maximum and minimum values of T according to GGIMFis sphalerite geothermometer general formula.

**Relative to mean T values of individual measurements.

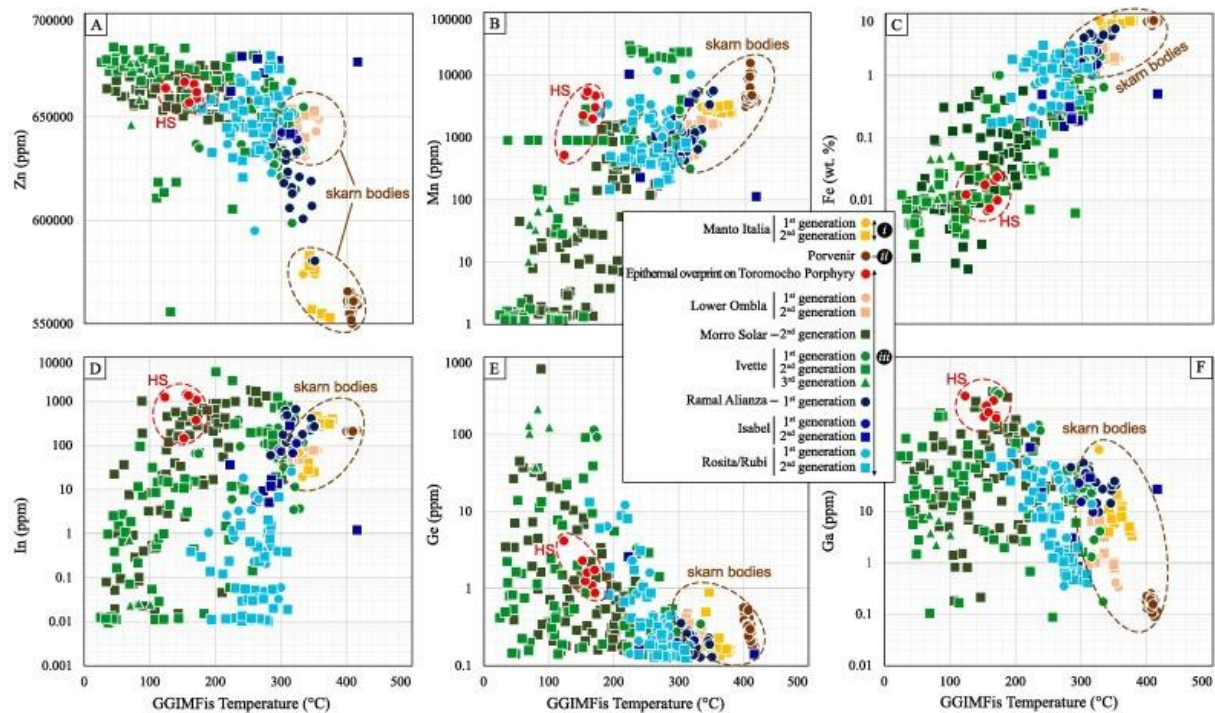


Fig. 14. Correlation between Zn, Mn, Fe, In, Ge, and Ga and GGIMFis T (Frenzel et al., 2016) in sphalerite from the Morococha district. Fields for studied sphalerite from *skarn* bodies (including low-sulfidation assemblages in Manto Italia and Porvenir, and intermediate-sulfidation assemblages in Lower Ombla) and from high-sulfidation assemblages (HS; epithermal veins overprinting the Toromocho stock) are highlighted. All other analyzed sphalerite comes from intermediate-sulfidation assemblages.

Available microthermometric data of fluid inclusions in the Morococha district by Catchpole et al. (2011) and Catchpole et al. (2015b) comprise fluid inclusion assemblages in i) quartz from milky quartz veins that cut the San Francisco stock, postdate the Manto Italia and Porvenir skarns and the Toromocho porphyry-type mineralization, and predate the studied Cordilleran mineralization; and ii) Stage C quartz, Fe-poor sphalerite (base-metal sub-stage), and rhodochrosite (carbonate sub-stage) in polymetallic Cordilleran veins. Fluid inclusions in the milky quartz veins, which can be considered representative of latest Toromocho porphyry fluids, yield homogenization temperatures (T_h) of $\sim 420^\circ$ to 410° °C. This temperature range compares well with the GGIMFis temperature for sphalerite from Porvenir and are higher than GGIMFis temperature for sphalerite from Manto Italia and Lower Ombla (Table 6). Although microthermometric data for fluid inclusions in the studied skarn-associated low-sulfidation assemblages at Porvenir and Manto Italia are unavailable, it can be assumed that they formed at temperatures slightly lower than 400° °C, typical for latest stage porphyry fluids. Therefore, the GGIMFis temperatures between 407° and 334° °C for sphalerite grains from Porvenir and Manto Italia are considered realistic within the large errors of the method.

As for the Cordilleran mineralization post-dating the Toromocho porphyry, primary fluid inclusion assemblages (FIAs) in the early base-metal sub-stage (Stage C) yield T_h in the range between 380° and 340° °C, and FIAs in the late carbonate sub-stage yield T_h in the range between 270° and 230° °C. Taking uncertainties into account, GGIMFis temperatures of sphalerite grains from Ramal Alianza fit the T_h of FIAs in the base-metal sub-stage. On the other hand, GGIMFis temperatures in sphalerite from porphyry-distal Rosita/Rubi match the T_h range of FIAs in the carbonate sub-stage. In contrast, significantly lower GGIMFis temperatures than those obtained by microthermometry, are found in 2nd (sl_{C2}) and 3rd (sl_{C3})-generation sphalerite grains from the Ivette manto and in sphalerite from high-sulfidation assemblages overprinting the Toromocho porphyry stock (Table 6).

6.3. Spatial and temporal distribution of In, Ge, and Ga in the polymetallic mineralization

The detailed study of the ore mineralogy and textures in different styles of polymetallic mineralization within the Morococha district reveals some patterns on the distribution of In, Ge, and Ga across the district (i.e., spatial control) and across the paragenetic sequences (i.e., temporal control). A note of caution has to be expressed as not all mineralized bodies studied here belong to a same event nor can be attributed to a same mineralizing center (the reader is referred to 2 Geological setting, 3.1 Sampling for details on the mineralization timing). So, we have studied low-sulfidation Stage A assemblages that have been formed during two mineralizing events significantly separate in time (“i” and “ii” in Section 3.1). Even for the studied intermediate- and high-sulfidation Stage C assemblages emplaced during the mineralizing event “iii” as part of the Morococha district-scale polymetallic event defined by Catchpole et al. (2015b), it cannot be excluded that in part derive from different feeders because they come from “physically” disconnected or independent ore bodies (see Fig. 2b in Catchpole et al., 2015b). Despite these limitations, our observations can serve as a first approximation to the relative variations in the

contents of these elements amongst assemblages formed throughout these stages; noteworthy, the GGIMFis geothermometer – which is based on minor and trace element contents in sphalerite – discussed in the previous section yields temperatures that broadly agree with the expected temperature drop from Stage A to Stage C in polymetallic mineralization. On the other hand, the GGIMFis temperatures of the studied Stage C sphalerite indicate a sustained decrease in temperature from porphyry-proximal to porphyry-distal assemblages thus suggesting that the observed trends are likely to be comparable with those in more “continuous” and simpler mineralized structures in other polymetallic districts.

The In content is relatively high in sphalerite from Stage A, low-sulfidation assemblages in polymetallic mineralization overprinting prograde exoskarn assemblages in Porvenir and Manto Italia (Fig. 9I) compared with most sphalerite from intermediate-sulfidation assemblages. However, the highest In content is associated with sphalerite from Stage C, high-sulfidation assemblages in epithermal veins overprinting the causative Toromocho stock. Regarding Stage C sphalerite in intermediate-sulfidation assemblages, the In content is higher in porphyry-proximal Morro Solar (located at the boundary between the Cu and Cu-Zn zones described by Catchpole et al., 2011) than in porphyry-distal Rosita/Rubí mineralization (located at the boundary between the Zn- Pb-Ag and Ag-Pb zones at depth; Fig. 1). Accordingly, the In content in Stage C sphalerite tends to decrease from porphyry-proximal to porphyry-distal zones at the district scale. Unlike In, the distribution patterns of Ge and Ga (Fig. 9J-K) in sphalerite from the different studied mineralized sites do not define clear trends on their spatial distribution. Of the studied minerals, galena is the other phase that records a consistent depletion in In from porphyry-proximal to porphyry-distal Cordilleran mineralization, albeit at much lower absolute values (Fig. 12B).

The correlation between trace-element contents and mineral position in the paragenetic sequences reflects that comparable high In content in sphalerite may occur in both Stage A (low-sulfidation) and Stage C (high- and intermediate-sulfidation) assemblages. In Stage C Cordilleran assemblages, In-rich sphalerite crystallized during the base-metal sub-stage (Fig. 6, Fig. 8) with early sphalerite generations enriched in In relative to late generations regardless of their location in the district (Fig. 9I). The drastic In depletion recorded in Ivette coincides with an abrupt increase of the Ge content to a maximum of 215 ppm in third-generation sphalerite (Fig. 9J). Gallium only shows limited depletion from early to late sphalerite within Stage C assemblages (Fig. 9K).

Similar trends in the spatial and temporal distributions of In as those described for Stage C sphalerite in Morococha have been recently identified in the sediment-hosted xenothermal Huari Huari and the volcanic dome-hosted epithermal Ánimas-Chocaya-Siete Suyos deposits in the Bolivian tin belt (Torró et al., 2019a, Torró et al., 2019b). In Huari Huari, the highest In contents in sphalerite were found in the vicinity of a *dacite* stock located at the center of the district and likely genetically related to the mineralization. In the Ánimas-Chocaya-Siete Suyos district, the highest In contents in sphalerite occur in the central area of the dome, where the main feeders of the system are located. In both districts, late generations of sphalerite, which crystallized in an intermediate-sulfidation stage, are systematically depleted in In relative to early generations of sphalerite (which attain up to 9 wt% In). Sahlström et al. (2017) describe a similar trend at the Mt Carlton high-sulfidation epithermal deposit in Australia, with higher In-(Ga) in the intrusion-proximal, Cu-rich zone relative to intrusion-distal (Ag-rich) zone. Therefore, the spatial and temporal patterns in the distribution of In revealed in Morococha are likely representative of intrusion-centered hydrothermal systems.

Yet, the controls behind such system-scale In patterns remain unclear. The work by Shimizu and Morishita (2012) sheds light on this question. This study proposes that fluids at temperatures in excess of 300 °C and enriched in In, Cu and to a lesser extent, in Sn and Ag, favored the crystallization of In-rich sphalerite in the Toyoha polymetallic deposit, and that In was either sourced from metal-rich magmatic fluids (see also Bauer et al., 2019b) or leached from preexisting Cu-rich ores. Intermediate-temperature (>250 °C) saline hydrothermal fluids would also favor the transport of In and Cu as chloride complexes (Seward et al., 2000, Schwarz-Schampera and Herzig, 2002). In summary, there are four main parameters that may apparently enhance In incorporation in sphalerite in hydrothermal systems: i) a sustained or punctual sourcing of In via metal-rich magmatic-hydrothermal fluids or pre-concentration in a Cu-rich ore predating the Zn-rich ore; ii) a relatively high availability of Cu – and of Ag and Sn – in the mineral system that enables the incorporation of In within the sphalerite crystal lattice through coupled substitutions; iii) a relatively high temperature of the mineralizing fluid (>250 °C); and iv) availability of Cl to form In (and Cu) chloride complexes.

The fact that the highest In contents are recorded in sphalerite from high-sulfidation assemblages in epithermal veins overprinting the causative Toromocho center (Fig. 9I), precipitated at distinctly low temperature (Table 6), suggests that the impact of temperature was probably secondary to other parameters such as the input of metal-rich magmatic-hydrothermal fluids. The progressive In depletion observed in distal-to-porphyry Zn-Pb-Ag and Ag-Pb Cordilleran mineralization and late generations of sphalerite from Stage C intermediate-sulfidation assemblages – regardless of their location in the district – would reflect crystallization from progressively more diluted fluids. Available fluid inclusion and stable isotope data for the Morococha district define, in addition to cooling, progressive dilution of a hydrothermal fluid of magmatic signature with meteoric water over its late-stage evolution (Catchpole et al., 2011, Catchpole et al., 2015b). On the other hand, trace-element determinations in inclusion fluids by the same authors revealed general Cu depletion from pre-Cordilleran to Cordilleran base-metal and carbonate stages, due to progressive Cu precipitation. Progressively more diluted and Cu-depleted mineralizing fluids precluded In concentration in late and distal to the porphyry center sphalerite.

6.4. General mineral chemistry trends – a principal component analysis

The principal component analysis (PCA) results of the log-transformed sphalerite trace element dataset are reported in Fig. 15. The first principal component (PC1), which explains a little more than 30% of the total variance (Fig. 15A), includes Fe and Co, characterized by positive signs and similar coefficients (Fig. 15C). PC2 is composed of Mn, Cd, Cu, Ga, In, and Sn. PC3 is a measure of Ge and Ag. PC2 was subdivided into two subgroups composed of Mn and Cd, and Cu, Ga, In, and Sn (Fig. 15D). In this perspective, Cu, In, Sn, and Ga, and to a lesser extent, Ge and Ag, group as a reflection of their positive correlations and paired participation in coupled substitutions.

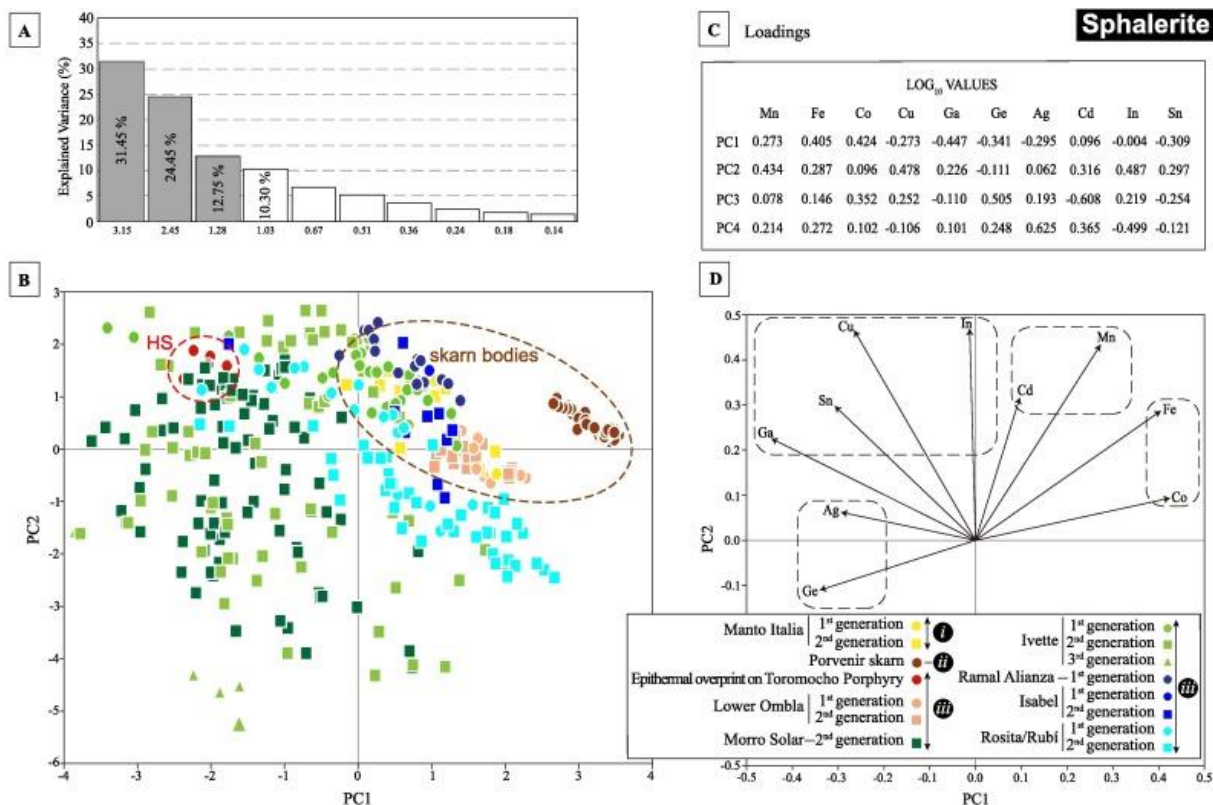


Fig. 15. Principal component analysis (PCA) of the log-transformed LA-ICP-MS data of trace element compositions in sphalerite from the Morococha district. A) Scree plot of the [eigenvalues](#) of the correlation matrix, explaining the variance. B) Plot of all data points corresponding to PC1 and PC2 for the trace element composition of sphalerites from all mineralizations. C) Loadings of the principal components (PC1 to PC4, explaining the 78.95% of the variance). D) Loading plots of the PCA showing the elements and framed groups of elements with similar behavior. “i”, “ii”, and “iii” refer to the mineralization events described in [Section 2.3](#) (Studied polymetallic mineralization styles in the Morococha district). Compositional fields for studied sphalerite from skarn bodies (Manto Italia, Porvenir, and Lower Ombla) and from high-sulfidation assemblages (HS; epithermal veins overprinting the Toromocho stock) are highlighted.

The results of PCA of the log-transformed chalcopyrite trace element dataset are shown in [Fig. 16](#). PC1 is formed by In, Ge, Ga, As, Sn, Co, Se, Bi, Mo, and Au, representing almost 38% of the variance ([Fig. 16A](#)). PC2 is composed of Zn, Cd, and Ag. PC3 is a measure of Hg and Tl. The PC1 vs. PC2 biplot ([Fig. 16D](#)) shows four clusters. PC1 was subdivided into three subgroups: a group formed by In, Ge, Ga, As, and Sn, another group composed of Bi, Se, and Co, and a third group constituted by Tl and Mo with PC3s, Mo and Au. Zinc, Cd, and Ag are positively correlated ([Fig. 16D](#)). Another positive correlation is between In, Ge, Ga, As, and Sn, highlighting that the incorporation of the three critical metals in the chalcopyrite crystal lattice requires the presence of Sn (especially for Ge), as well as Ag (for In and Ga), to form coupled substitutions. The elements Se, Co, and Bi, are fairly correlated. The most noteworthy example is reflected in the first and second-generation chalcopyrite grains from Lower Ombla with higher Co and Se in the first-generation, supported by the presence of sphalerite “stars” (i.e., high-temperature; [Fig. 3B](#)).

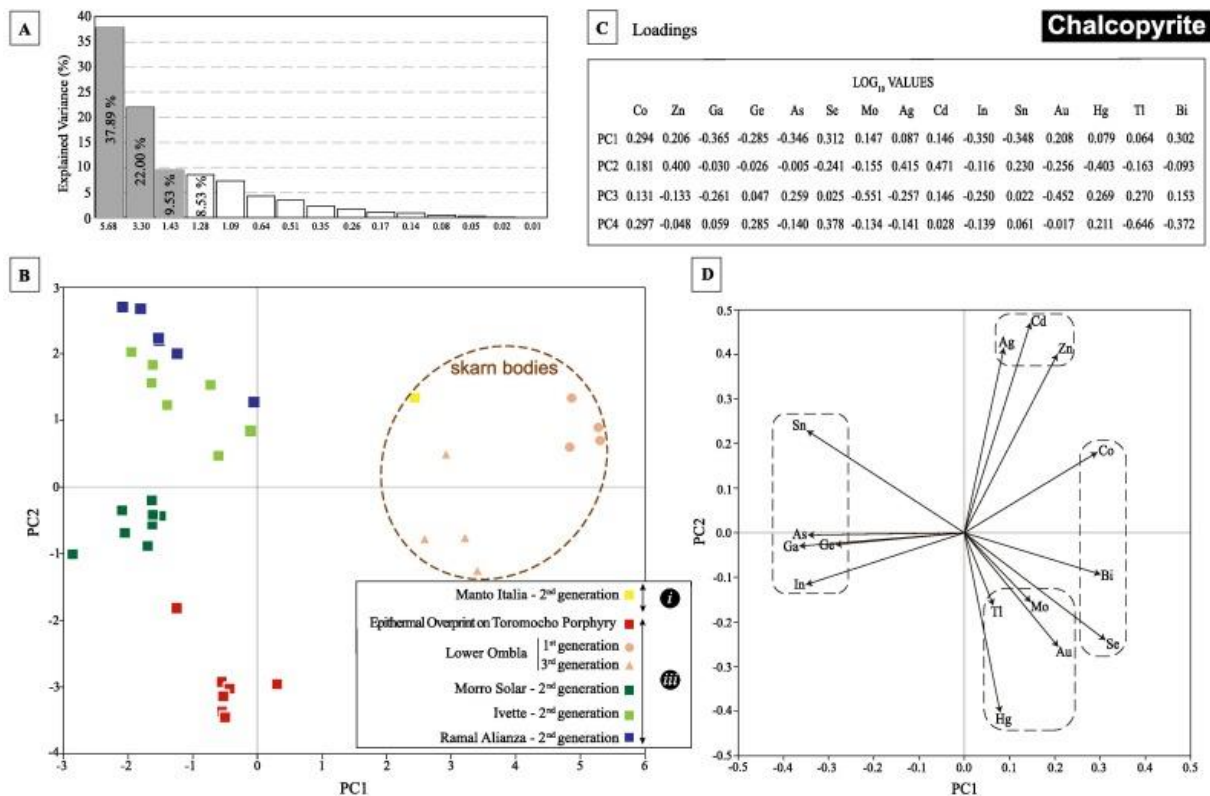


Fig. 16. Principal component analysis (PCA) of the log-transformed LA-ICP-MS data of trace element compositions in chalcopyrite from the Morococha district. A) Scree plot of the *eigenvalues* of the correlation matrix, explaining the variance. B) Plot of all data points corresponding to PC1 and PC2 for the trace element composition of sphalerites from all mineralizations. C) Loadings of the principal components (PC1 to PC4, explaining the 77.95% of the variance). D) Loading plots of the PCA showing the elements and framed groups of elements with similar behavior. “i”, “ii”, and “iii” refer to the mineralization events described in Section 2.3 (Studied polymetallic mineralization styles in the Morococha district). The compositional field for studied sphalerite from skarn bodies (Manto Italia and Lower Ombla) is highlighted.

PCA for the Morococha sphalerite and chalcopyrite dataset allows for an overview of the minor and trace-element composition of these two phases throughout the studied polymetallic mineralization in the Morococha porphyry district. Sphalerite grains from the polymetallic mineralization overprinting prograde exoskarn mineralization (i.e., Porvenir, Manto Italia, and Lower Ombla) are particularly enriched in Co and depleted in Ge, Ga, and Ag relative to sphalerite grains from the Cordilleran mineralization, and these elements do not show apparent correlation with In or Cu (Fig. 15B). Chalcopyrite grains from polymetallic mineralization overprinting prograde exoskarn mineralization show also distinctive enrichment in Co and are depleted in Ge, Ga, As, and In (Fig. 16B). Regarding Stage C sphalerite, grains in high-sulfidation assemblages overprinting the Toromocho stock, and early generations in proximal-to-porphyry, intermediate-sulfidation assemblages are enriched in In and Cu – and to a lesser extent in Ga – relative to early generations in distal-to-porphyry mineralization (see also Fig. 9). Chalcopyrite from high- and intermediate-sulfidation assemblages in Cordilleran mineralization yield, from distal to proximal locations, enrichment in Se and Hg and depletion in Sn and Ag (see also Fig. 11).

7. Conclusions and implications

In this study, systematic trace element determinations have been conducted in sphalerite, chalcopyrite, galena, and tetrahedrite-tennantite from different polymetallic mineralization styles within the Morococha district, Peru. Studied mineralization styles and assemblages include i) low-sulfidation polymetallic assemblages overprinting magnetite-serpentine exoskarn at Manto Italia and Porvenir massive replacement bodies (equivalent to Stage A in Cordilleran-type deposits); ii) high-sulfidation epithermal veins overprinting the causative Toromocho porphyry stock (i.e., Stage C of Cordilleran-type deposits); and iii) skarn and skarn-free intermediate-sulfidation polymetallic mineralization from Cu and Cu-Zn (i.e., proximal to porphyry; Lower Ombla, Morro Solar and Ivette) and Zn-Pb-Ag and Pb-Ag (i.e., distal to porphyry; Ramal Alianza, Isabel, Rosita/Rubí) ore bodies and veins (i.e., Stage C of Cordilleran-type deposits). Detailed *petrography* and mineral *geochemistry* in ore samples from these sites reveal some trace-element distribution patterns involving the high-tech metals In, Ge, and Ga across the district and along paragenetic sequences (i.e., stages of mineralization).

Indium is mostly concentrated in sphalerite (217–2.7 ppm, up to 4608 ppm) and chalcopyrite (109–32 ppm, up to 1070 ppm), and much less concentrated in tetrahedrite-tennantite and galena. In coeval generations, the In content in sphalerite is at least 2 times higher than in chalcopyrite. Gallium also concentrates preferentially in sphalerite (61–2.0 ppm, up to 2137 ppm) and in chalcopyrite (62–1.5 ppm, up to 630 ppm), and significantly less in tetrahedrite-tennantite and galena. *Germanium* is systematically very low in all four investigated minerals (1.2–0.20 ppm) with some anomalous values in sphalerite up to 701 ppm.

The content of the three elements varies significantly across the district and across the generations identified for individual minerals in each mineralized site. The In content is systematically high in sphalerite from Stage A low-sulfidation assemblages in polymetallic skarns. Stage C high-sulfidation assemblages overprinting the Toromocho porphyry host sphalerite with the highest In content. In Stage C intermediate-sulfidation assemblages, sphalerite yields higher In values in proximal-to-porphyry (Cu and Zn-Cu zones) than in distal-to-porphyry (Zn-Pb-Ag and Pb-Ag zones) mineralization. In the same assemblages, the In content also decreases in galena with increasing distances from the hydrothermal center. On the other hand, the In content decreases from early to late generations of Stage C sphalerite, coupled with an increase in the Ge content, with the highest values of this element recorded in late Fe-poor, low-temperature sphalerite forming colloform aggregates.

For Stage C assemblages in Cordilleran mineralization emplaced during the “Morococha district-scale polymetallic event” of [Catchpole et al. \(2015b\)](#) post-dating the porphyry mineralization at Toromocho, trace-element mineral compositions suggests the following trends from porphyry-proximal to porphyry-distal Cordilleran mineralization: i) in sphalerite, In and Cu (and to a lesser extent, Ga) depletion; ii) in chalcopyrite, Se and Hg depletion and Sn and Ag enrichment; complementarily, iii) in galena, In depletion; and iv) in tetrahedrite-tennantite, Ag enrichment.

The GGIMFis sphalerite geothermometer of [Frenzel et al. \(2016\)](#) has been tested using our Morococha dataset and comparing the obtained temperatures with available fluid inclusion microthermometric data. The GGIMFis geothermometer yields mostly plausible temperature ranges and general temperature decrease from Stage A to Stage C assemblages. In Stage C intermediate-sulfidation assemblages of the “Morococha district-scale polymetallic event”, there is a sustained drop in the GGIMFis temperatures from proximal-to-porphyry to distal locations and from early to late sphalerite generations.

The strong positive correlation between In and Cu in sphalerite points to $\text{Cu}^+ + \text{In}^{3+} \leftrightarrow 2\text{Zn}^{2+}$ coupled substitution as the principal mechanism for the incorporation of In within the crystal lattice. Cationic correlations in sphalerite also support $\text{Cu}^+ + \text{Ga}^{3+} \leftrightarrow 2\text{Zn}^{2+}$ and probably additional $(\text{Sn}, \text{Ge})^{4+} + (\text{Ga}, \text{In})^{3+} + (\text{Cu} + \text{Ag})^+ \leftrightarrow 4\text{Zn}^{2+}$ coupled substitutions. Copper is involved in all these substitution schemes and hence its availability in the mineral system defines the spatial and [temporal distribution](#) of In and Ga in sphalerite. Therefore, our data indicate that a high availability of Cu in metal-rich magmatic-hydrothermal fluids may enhance In enrichment in sphalerite.

Declaration of Competing Interest

The authors declare that they have no known competing financial interests or personal relationships that could have appeared to influence the work reported in this paper.

Acknowledgments

This study was economically supported by the Peruvian CONCYTEC-FONDECYT-World Bank project 107-2018-FONDECYT-BM-IADT-AV, the FONCAI-0023-2019 project granted by the Pontificia Universidad Católica del Perú (PUCP) and a Huiracocha Ph. D grant to D.B. granted by the PUCP. Pan American Silver Corp. provided field and logistical support and access to the mine area. Pan American Silver Corp. Morococha staff is most gratefully acknowledged, particularly Julio Zárate and Rubén Diaz. We appreciate the technical support by Xavier Llovet (CCiT-UB) during the acquisition of EPMA data, and by Peter Tollan (ETHZ) during the acquisition of LA-ICP-MS data. We are grateful to Fredrik Sahlström, Max Frenzel, and Editor-in-Chief Franco Pirajno for their constructive comments which significantly improved the manuscript.

References

- Ageneau, M., 2008. Genesis of Ag-rich mineralization in the Buenaventura and Galera veins, Yacumina zone, SW part of the Morococha district, central Peru. M.Sc. thesis. University of Geneva, Geneva, Switzerland. p. 119.
- Armbruster, T., Makovicky, E., Berlepsch, P., Sejkora, J., 2003. Crystal structure, cation ordering, and polytypic character of diaphorite, $\text{Pb}_2\text{Ag}_3\text{Sb}_3\text{S}_8$, a PbS-based structure. *Eur. J. Mineral.* 15, 137–146.
- Barton, P.B., Bethke, P.M., 1987. Chalcopyrite disease in sphalerite; pathology and epidemiology. *Am. Mineral.* 72, 451–467.
- Bauer, M.E., Seifert, T., Burisch, M., Krause, J., Richter, N., Gutzmer, J., 2019a. Indium-bearing sulfides from the Hammerlein skarn deposit, Erzgebirge, Germany: Evidence for late-stage diffusion of indium into sphalerite. *Miner. Deposita* 54, 175–192.
- Bauer, M.E., Burisch, M., Ostendorf, J., Krause, J., Frenzel, M., Seifert, T., Gutzmer, J., 2019b. Trace element geochemistry of sphalerite in contrasting hydrothermal fluid systems of the Freiberg district, Germany: insights from LA-ICP-MS analysis, near-isotope geochemistry. *Miner. Deposita* 54, 237–262.
- Baumgartner, R.J., Van Kranendonk, M.J., Pagès, A., Fiorentini, M.L., Wacey, D., Ryan, C., 2020. Accumulation of transition metals and metalloids in sulfidized stromatolites of the 3.48 billion-year-old Dresser Formation, Pilbara Craton. *Precamb. Res.* 337, 105534.
- Belissant, R., Munoz, M., Boiron, M.C., Luais, B., Mathon, O., 2019. Germanium crystal chemistry in Cu bearing sulfides from micro-XRF mapping and micro-XANES spectrometry. *Minerals* 9, 227.
- Benavides, V., 1999. Orogenic evolution of the Peruvian Andes: the Andean Cycle. In: Skinner, B.J. (Ed.), *Geology and Ore Deposits of the Central Andes*. Society of Economic Geologists Special Publication, pp. 61–107.
- Bendezú, A., Catchpole, H., Kouzmanov, K., Fontboté, L., Astorga, C., 2008. Miocene magmatism and related porphyry and polymetallic mineralization in the Morococha district, central Peru. *Sociedad Geológica del Perú, XIII Congreso Latinoamericano de Geología*, Lima, Peru, September 29–October 3, 2008, Proceedings.
- Bendezú, A., Kouzmanov, K., Ovtcharova, M., Spikings, R., Fontboté, L., 2012. Timing of porphyry emplacement in the Miocene Morococha district, central Peru: U-Pb and Ar-Ar geochronological record. In: *International Geological Congress, 34th Brisbane, Australia 2012*, pp. 1–6.
- Beuchat, S., 2003. Geochronological, structural, isotopes and fluid inclusion constraints of the polymetallic Domo de Yauli district, Peru. *Terre Environ.* 41, 130.
- Bissig, T., Ullrich, T., Tosdal, R., Friedman, R., Ebert, S., 2008. The time-space distribution of Eocene to Miocene magmatism in the central Peruvian polymetallic province and its metallogenic implications. *J. S. Am. Earth Sci.* 26, 16–35.
- Bonnet, J., Mosser-Ruck, R., Caumon, M.C., Rouer, O., Andre-Mayer, A.S., Cauzid, J., Peifert, C., 2016. Trace element distribution (Cu, Ga, Ge, Cd and Fe) in sphalerite from the Tennessee MVT deposits, USA, by combined EMPA, LA-ICP-MS, Raman spectroscopy and crystallography. *Can. Mineral.* 54, 1261–1284.
- Catchpole, H., 2011. Porphyry-related polymetallic mineralisation in the Morococha district, central Peru: mineralisation styles, timing and fluid evolution. Ph. D. Thesis, University of Geneva. *Terre & Environment*, 102, 192 + 86.
- Catchpole, H., Kouzmanov, K., Fontboté, L., Guillong, M., Heinrich, C.A., 2011. Fluid evolution in zoned Cordilleran polymetallic veins—insights from microthermometry and LA-ICP-MS of fluid inclusions. *Chem. Geol.* 281, 293–304.
- Catchpole, H., Kouzmanov, K., Fontboté, L., 2012. Copper-excess stannoidite and tennantite-tetrahedrite as proxies for hydrothermal fluid evolution in a zoned Cordilleran base metal district, Morococha, central Peru. *Can. Mineral.* 50, 719–743.
- Catchpole, H., Kouzmanov, K., Bendezú, A., Ovtcharova, M., Spikings, R., Stein, H., Fontboté, L., 2015a. Timing of porphyry (Cu-Mo) and base metal mineralization (Zn-Pb-Ag-Cu) in a magmatic-hydrothermal system—Morococha district. *Peru. Miner. Deposita* 50, 895–922.

- Catchpole, H., Kouzmanov, K., Putlitz, B., Seo, J., Fontboté, L., 2015b. Zoned base metal mineralization in a porphyry system: Origin and evolution of mineralizing fluids in the Morococha District. *Peru. Econ. Geol.* 110, 39–71. de Pasco, C., Corporation, C., 1948. Lead and zinc deposits of the Cerro de Pasco Corporation in central Peru. In: 18th International Geological Congress, Great Britain, Part VII, pp. 154–186. Chinalco Mining Corporation International, 2015. Annual Report, Lima, pp. 12–35. <<https://www.lhcxnews.hk/listedco/listconews/sehk/2016/0428/ltm20160428325.pdf>>.
- Cook, N.J., Ciobanu, C.L., Pring, A., Skinner, W., Shimizu, M., Danyushevsky, L.V., Saini-Eidukat, B., Melcher, F., 2009. Trace and minor elements in sphalerite: a LA-ICPMS study. *Geochim. Cosmochim. Acta* 73, 4761–4791.
- Cook, N.J., Ciobanu, C., Williams, T., 2011a. The mineralogy and mineral chemistry of indium in sulphide deposits and implications for mineral processing. *Hydrometallurgy* 108, 226–228.
- Cook, N.J., Sundblad, K., Valkama, M., Nygård, R., Ciobanu, C.L., Danyushevsky, L., 2011b. Indium mineralisation in A-type granites in southeastern Finland: insights into mineralogy and partitioning between coexisting minerals. *Chem. Geol.* 284, 62–73.
- Cook, N.J., Ciobanu, C.L., Brugger, J., Etschmann, B., Howard, D.L., de Jonge, M.D., Ryan, C.G., Paterson, D.J., 2012. Determination of the oxidation state of Cu in substituted Cu-In-Fe-bearing sphalerite via μ -XANES spectroscopy. *Am. Mineral.* 97, 476–479.
- Cook, N.J., Ciobanu, C.L., 2015. Mineral hosts for critical metals in hydrothermal ores [ext. abs.]. In: Biennial Meeting of the Society for Geology Applied to Mineral Deposits, 13th, Nancy, France, 2015, Extended Abstracts, pp. 707–710.
- Di Benedetto, F., Bernardini, G.P., Costagliola, P., Plant, D., Vaughan, D.J., 2005. Compositional zoning in sphalerite crystals. *Am. Mineral.* 90, 1384–1392. European Commission, 2017. Critical Raw Materials. <https://ec.europa.eu/growth/sec-tors/raw-materials/specific-interest/critical_en>.
- Eyzaguirre, V., Montoya, D., Silberman, M., Noble, D., 1975. Age of igneous activity and mineralization, Morococha district, central Peru. *Econ. Geol. Bull. Soc. Econ. Geol.* 70, 1123–1125.
- Fontboté, L., 2018. Ore deposits of the Central Andes. *Elements* 14, 257–261.
- Fontboté, L., 2020. Systematic trends in the evolution of porphyry-related Zn-Pb-(Ag) deposits. Swiss Geoscience Meeting. 18th, Zurich, Switzerland, 2020. Extended Abstracts.
- Foord, E.E., Shawe, D.R., Conklin, N.M., 1988. Coexisting galena, PbS and sulfosalts: evidence for multiple episodes of mineralization in the Round Mountain and Manhattan gold districts, Nevada. *Can. Mineral.* 26, 355–376.
- Frenzel, M., Hirsch, T., Gutzmer, J., 2016. Gallium, germanium, indium, and other trace and minor elements in sphalerite as a function of deposit type—a meta-analysis. *Ore Geol. Rev.* 76, 52–78.
- Frenzel, M., Mikolajczak, C., Reuter, M.A., Gutzmer, J., 2017. Quantifying the relative availability of high-tech by-product metals: the cases of gallium, germanium and indium. *Resour. Policy* 52, 327–335.
- Frenzel, M., Bachmann, K., Carvalho, J.R.S., Relvas, J.M.R.S., Pacheco, N., Gutzmer, J., 2019. The geometallurgical assessment of by-products: geochemical proxies for the complex mineralogical department of indium at Neves-Corvo, Portugal. *Miner. Deposita* 54, 959–982.
- Gemrich, L., Torrío, L., Melgarejo, J.C., Laurent, O., Vallance, J., Chelle-Michou, C., Sempere, T.P.A., 2021. Trace element composition and U-Pb ages of cassiterite from the Bolivian tin belt. *Miner. Deposita* (in press).
- George, L., 2013. In: Trace and Minor Elements in Galena: A Reconnaissance LA-ICP-MS study: Honours degree in Geology thesis. The University of Adelaide, Adelaide, Australia, p. 133.
- George, L., Cook, N.J., Cristiana, L., Wade, B.P., 2015. Trace and minor elements in galena: a reconnaissance LA-ICP-MS study. *Am. Mineral.* 100, 548–569.
- George, L.L., Cook, N.J., Crowe, B.B.P., Ciobanu, C.L., 2018. Trace elements in hydrothermal chalcocopyrite. *Mineral. Mag.* 82, 59–88. Goldfarb, R.J., Hofstra, A.H., Simmons, S.F., 2016. Critical elements in carlin, epithermal, and orogenic gold deposits. *Rev. Econ. Geol.* 18, 217–244.
- Graeser, S., 1969. Minor elements in sphalerite and galena from Binnatal. *Contrib. Mineral. Petr.* 24, 156–163. Guberman, D., 2015. Germanium: U.S. Geological Survey Mineral Commodity Summaries 2015, pp. 64–65. <<https://minerals.usgs.gov/minerals/pubs/mcs/2015/mcs2015.pdf>>.
- Guillong, M., Hametner, K., Reusser, E., Wilson, S.A., Günther, D., 2005. Preliminary Characterisation of New Glass Reference Materials (GSA-1G, GSC-1G, GSD-1G and GSE-1G) by Laser Ablation-Inductively Coupled Plasma-Mass Spectrometry Using 193 nm, 213 nm and 266 nm Wavelengths. *Geostand. Geoanal. Res.* 29, 315–331.
- Guillong, M., Meier, D.L., Allan, M.M., Heinrich, C.A., Yardley, B.W.D., 2008. SILLS: A MATLAB-based program for the reduction of laser ablation ICP-MS data of homogeneous materials and inclusions. In: Sylvester, P. (Ed.), *Laser Ablation ICP-MS in the Earth Sciences: Current Practices and Outstanding Issues*. Mineralogical Association of Canada, Vancouver, pp. 328–333.
- Guillong, M., Wotzlav, J.F., Looser, N., Laurent, O., 2020. Evaluating the reliability of U-Pb laser ablation inductively coupled plasma mass spectrometry (LA-ICP-MS) carbonate geochronology: matrix issues and a potential calcite validation reference material. *Geochronology* 2, 155–167. <<https://doi.org/10.5194/gchron-2-155-2020>>.
- Haapala, P.S., 1953. Morococha anhydrite: Sociedad Geológica Perú. *Bulletin* 26, 21–32.
- Heuschmidt B, La Torre J.B., Angels V.M., Zapata, M.C., 2002. Las áreas prospectivas de Bolivia para yacimientos metalíferos. *Boletín del Servicio Nacional de Geología y Minería*, 30. ISSN 1023-7674.
- Jaskula, B.W., 2015. Gallium: USGS Mineral Commodity Summaries. January 2015, pp. 58–59.
- Jochum, K.P., Weis, U., Stoll, B., Kuzmin, D., Yang, Q., Raczek, I., Jacob, D.E., Stracke, A., Birbaum, K., Frick, D.A., Günther, D., Enzweiler, J., 2011. Determination of reference values for NIST SRM 610–617 glasses following ISO guidelines, *Geostand. Geoanal. Res.* 35, 397–429.
- Johan, Z., 1988. Indium and germanium in the structure of sphalerite: an example of coupled substitution with copper. *Miner. Petrol.* 39, 211–229.
- John, D.A., Taylor, R.D., 2016. By-products of porphyry copper and molybdenum deposits. *Rev. Econ. Geol.* 18, 137–164.
- Klekovkina, V.V., Gainov, R.R., Vagizov, F.G., Dooglav, A.V., Golovanevskiy, V.A., Pen'kov, I.N., 2014. Oxidation and magnetic states of chalcocopyrite CuFeS₂: a first principles calculation. *Opt. Spectrosc.* 116, 885–888. Kobe, H.W., 1990. Stratabound sulfide occurrences in the Paleozoic of the Yauli Dome, Central Peru. A summary. In: Fontboté, L., Amstutz, G.C., Cardozo, M., Cedillo, E., Frutos, J. (Eds.), *Stratabound Ore Deposits in the Andes*: Berlin. Springer-Verlag, pp. 113–122.
- Korges, M., Weis, P., Lüders, V., Laurent, O., 2020. Sequential evolution of Sn-Zn-In mineralization at the skarn hosted Hammerlein deposit, Erzgebirge, Germany, from fluid inclusions in ore and gangue minerals. *Miner. Deposita* 55, 937–952.
- Kouzmanov, K., Ovtcharova, M., von Quadt, A., Guillong, M., Spikings, R., Schaltegger, U., Fontboté, L., Rivera, L., 2008. U-Pb and 40Ar/39Ar age constraints for the timing of magmatism and mineralization in the giant Toromocho porphyry Cu-Mo deposit, central Peru [ext. abs.]. In: Congreso Latinoamericano de Geología, 13th, Lima, Peru, 2008, Proceedings, p. 6.
- Kouzmanov, K., Chiaradia, M., Fontboté, L., Spangenberg, J., 2011. Origin of massive anhydrite bodies in the Morococha district, central Peru: insights from stable (O, S) and radiogenic (Sr, Nd) isotope geochemistry. In: Barra, F., Reich, M., Campos, F., Tornos, F. (Eds.), *Biennial Meeting of the Society for Geology Applied to Mineral Deposits*, 11th, Antofagasta, Chile, 2011, Extended Abstracts, pp. 405–407.
- Le coq de Boisbaudran, P.E., 1875. Caractères chimiques et spectroscopiques d'un nouveau métal, le gallium, découvert dans une blende de la mine de Pierrefitte, vall'ée d'Argel'ès (Pyr'énées). *C. R. Hebdomadaires des S'éances de l'Acad. Sci.* 81, 493–49.
- Lee, C.-T.A., Tang, M., 2020. How to make porphyry copper deposits. *Earth Planet. Sc. Lett.* 529, 1–11.
- Lepry, L.A.J., 1981. The structural geology of the Yauli dome region, Cordillera Occidental, Peru. M.Sc. thesis. University of Arizona, Tucson, United States, p. 100.
- Li, Y., Kawashima, N., Li, J., Chandra, A.P., Gerson, A.R., 2013. A review of the structure, and fundamental mechanisms and kinetics of the leaching of chalcocopyrite. *Adv. Colloid Interface Sci.* 197, 1–32.
- Liu, W., Cook, N.J., Ciobanu, C.L., Guilbert, S.E., 2019. Trace element substitution and grain-scale compositional heterogeneity in enargite. *Ore Geol. Rev.* 111, 103004.
- Lockington, J.A., Cook, N.J., Ciobanu, C.L., 2014. Trace and minor elements in sphalerite from metamorphosed sulphide deposits. *Mineral. Petrol.* 108, 873–890. McLaughlin, D., 1924. The Geology and Physiography of the Peruvian Cordillera, departments of Junin and Lima. *GSA Bull.* 35, 591–632.
- McLaughlin, D.H., Graton, L.C., 1935. Copper in the Cerro de Pasco and Morococha districts. In: *International Geological Congress*, 16th. Washington, USA. Department of Junin, Peru, pp. 513–544.
- Megard, F., 1968. Geología del cuadr'angulo de Huancayo, Servicio de Geología y Minería. *Boletín* 18, 1–105.
- Meinert, L.D., 2005. World skarn deposits. In: Hedenquist, J.W., Thompson, J.F.H., Goldfarb, R.J., Richards, J.P. (Eds.), *100th Anniversary volume*: Littleton, Society of Economic Geologists, pp. 299–336.
- Mikhlin, Y., Tomashevich, Y., Tauson, V., Vyalikh, D., Molodtsov, S., Szargan, R., 2005. A comparative X-ray absorption near-edge structure study of bornite, Cu₅FeS₄, and chalcocopyrite, CuFeS₂. *J. Electron Spectrosc.* 142, 83–88.

- Moritz, R., Beuchat, S., Chiaradia, M., Sallier, B., Lisboa, H., Stucky, P., 2001. Zn-Pb mantos and veins at Domo de Yauli, central Peru: Two products of one hydrothermal system with common Pb & S sources, but contrasting fluid inclusion characteristics [ext abs.]. In: Biennial Meeting of the Society for Geology Applied to Mineral Deposits, pp. 173–176.
- Murakami, H., Ishihara, S., 2013. Trace elements of indium-bearing sphalerite from tin polymetallic deposits in Bolivia, China and Japan: a femto-second LA-ICPMS study. *Ore Geol. Rev.* 53, 223–243.
- Noble, D., McKee, E., 1999. The Miocene metallogenic belt of central and northern Peru. In: Skinner, B.J. (Ed.), *Geology and Ore Deposits of the Central Andes*. Society of Economic Geologists Special Publication, pp. 155–193.
- Oen, I.S., Kager, P., Kieft, C., 1980. Oscillatory zoning of a discontinuous solid-solution series: Sphalerite-stannite. *Am. Mineral.* 65, 1220–1232.
- Oftedal, I., 1940. Untersuchungen über die Nebenbestandteile von Erzmineralien norwegischer zinnblendeführender Vorkommen. *Skrift. Norsk Vidensk. Akad. Oslo. Math. Naturv.* 8, 1–103.
- Parasyuk, O.V., Voronyuk, S.V., Gulay, L.D., Davidyuk, G.Y., Halka, V.O., 2003. Phase diagram in the of the CuInS–ZnS system and some physical properties of solid solutions phases. *J. Alloy. Compd.* 348, 57–64.
- Pearce, C.I., Patrick, R.A.D., Vaughan, D.J., Henderson, C.M.B., van der Laan, G., 2006. Copper oxidation state in chalcopyrite: Mixed Cu d9 and d10 characteristics. *Geochim. Cosmochim. Acta* 70, 4635–4642.
- Perez, J., Kouzmanov, K., Fontbote, L., Astorga, C., 2011. Mineralization, structural, and geochemical characteristics of the Toldojirca prospect and the San Andrés vein, Morococha district, central Peru. In: Society for Geology Applied to Mineral Deposits (SGA) 11th biennial Meeting, pp. 247–249. Petersen, U., 1965. Regional geology and major ore deposits of Central Perú. *Econ. Geol. Bull. Soc. Econ. Geol.* 60, 407–476.
- Pring, A., Wade, B., McFadden, A., Lenehan, C.E., Cook, N.J., 2020. Coupled substitutions of minor and trace elements in co-existing sphalerite and wurtzite. *Minerals* 10, 147.
- Ramdohr, P., 1980. In: *The Ore Minerals and their Intergrowths*. Pergamon Press, Berlin, p. 1205.
- Renock, D., Becker, U., 2011. A first principles study of coupled substitution in galena. *Ore Geol. Rev.* 42, 71–83.
- Reich, F., Richter, T., 1863. Ueber das Indium. *Prakt. Chem.* 90, 172–176.
- Reich, M., Román, N., Barra, F., Morata, D., 2020. Silver-rich chalcopyrite from the active Cerro Pabellón Geothermal System, northern Chile. *Minerals* 10, 113.
- Richards, J.P., 2009. Post-subduction porphyry Cu–Au and epithermal Au deposits: products of remelting of subduction-modified lithosphere. *Geology* 37, 247–250.
- Ritterbush, K.A., Ibarra, Y., Bottjer, D.J., Corsetti, F.A., Rosas, S., West, A.J., Berelson, W. M., Yager, J.A., 2015. Marine ecological state-shifts following the Triassic Jurassic mass extinction. In: *Paleontological Society Papers*, pp. 121–136.
- Rosas, S., 1994. Facies, diagenetic evolution, and sequence analysis along a SW-NE profile in the southern Pucará basin (Upper Triassic-Lower Jurassic), central Peru. *Heidelberger Geowiss. Abh.* 80, 337.
- Rosas, S., Fontbote, L., Morche, W., 1996. Within-plate volcanism in Upper Triassic to Lower Jurassic Pucara Group carbonates (central Peru) [ext. abs.]. In: *International Symposium on Andean Geodynamics (ISAG)*, 3rd, Saint Malo, France, 1996, Extended Abstracts, pp. 641–644.
- Rosas, S., Fontboté, L., Tankard, A., 2007. Tectonic evolution and paleogeography of the Mesozoic Pucará Basin, central Peru. *J. S. Am. Earth Sci.* 24, 1–24.
- Rottier, B., Kouzmanov, K., Walle, M., Bendežú, R., Fontbote, L., 2016. Sulfide replacement processes revealed by textural and LA-ICP-MS trace element analyses: example from the early mineralization stages at Cerro de Pasco, Peru. *Econ. Geol.* 111, 1347–1367.
- Rottier, B., Kouzmanov, K., Casanova, V., Walle, M., Fontbote, L., 2018. Cyclic dilution of magmatic metal-rich hypersaline fluids by magmatic low-salinity fluid: A major process generating the giant epithermal polymetallic deposit of Cerro de Pasco, Peru. *Econ. Geol.* 113, 825–856.
- Rytuba, J.J., John, D.A., Foster, A., Ludington, S.D., Kotlyar, B., 2003. Hydrothermal enrichment of gallium in zones of advanced argillic alteration: examples from the Paradise Peak and McDermitt ore deposits, Nevada. In: Bliss, J.D., Moyle, P.R., Long, K.R. (Eds.), *Contributions to Industrial-mineral Research*. US Department of the Interior, US Geological Survey, p. 16.
- Sack, R.O., Goodell, P.C., 2002. Retrograde reactions involving galena and Ag-sulfosalts in a zoned ore deposit, Julcani, Peru. *Mineral. Mag.* 66, 1043–1062.
- Sack, R.O., 2005. Internally consistent database for sulfides and sulfosalts in the system Ag₂S–Cu₂S–ZnS–FeS–Sb₂S₃–As₂S₃. *Geochim. Cosmochim. Acta* 69, 1157–1164.
- Sack, R.O., Ebel, D.S., 2006. Thermochemistry of sulfide mineral solutions, Sulfide Mineralogy and Geochemistry. *Rev. Mineral. Geochem.* 61, 265–364.
- Sack, R.O., Lichtner, P.C., 2009. Constraining compositions of hydrothermal fluids in equilibrium with polymetallic ore forming sulfide assemblages. *Econ. Geol. Bull. Soc. Econ. Geol.* 104, 1249–1264.
- Sahlstrom, F., Arribas, A., Dirks, P., Corral, I., Chang, Z., 2017. Mineralogical distribution of germanium, gallium and indium at the Mt Carlton high-sulfidation epithermal deposit, NE Australia and comparison with similar deposits worldwide. *Minerals* 7, 213.
- Saintilan, N.J., Sproson, A.D., Selby, D., Rottier, B., Casanova, V., Creaser, R.A., Kouzmanov, K., Fontbote, L., Piecha, M., Gereke, M., Zambito IV, J.J., 2021. Osmium isotopic constraints on sulphide formation in the epithermal environment of magmatic-hydrothermal mineral deposits. *Chem. Geol.* 564, 120053.
- Savard, D., 2018. UQAC (Université du Québec à Chicoutimi) FeS-1 <<https://sulfidslase.ripcms.wordpress.com/rm-available/>>.
- Scherrenberg, A.F., Kohn, B.P., Holcombe, R.J., Rosenbaum, G., 2016. Thermotectonic history of the Marañón Fold-Thrust Belt, Peru: insights into mineralization in an evolving orogen. *Tectonophysics* 667, 16–36.
- Schorr, S., Wagner, G., 2005. Structure and phase relations of the Zn_{2x}(CuIn)_{1-x}S₂ solid solution series. *J. Alloy. Compd.* 396, 202–207.
- Schulz, K.J., DeYoung Jr., J.H., Seal II, R.R., Bradley, D.C., 2017. Critical mineral resources of the United States – economic and environmental geology and prospects for future supply. In: *U.S. Geological Survey Professional Paper*, p. 797.
- Schwarz-Schampera, U., Herzig, P., 2002. In: *Indium: Geology, Mineralogy, and Economics*. Springer, Heidelberg, p. 216.
- Seward, T.M., Henderson, C.M.B., Charnock, J.M., 2000. Indium (III) chloride complexing and solvation in hydrothermal solutions to 350 °C: An EXAFS study. *Chem. Geol.* 167, 117–127.
- Shimizu, T., Morishita, Y., 2012. Petrography, chemistry, and near-infrared microthermometry of indium-bearing sphalerite from the Toyoha polymetallic deposit, Japan. *Econ. Geol.* 107, 723–735.
- Sillitoe, R.H., 2010. Porphyry Copper Systems. *Econ. Geol. Bull. Soc. Econ. Geol.* 105, 3–41.
- Skirrow, R.G., Huston, D.L., Mernagh, T.P., Thorne, J.P., Dulfer, H., Senior, A.B., 2013. In: *Critical Commodities for a High-tech World: Australia's Potential to Supply Global Demand*. Geoscience Australia, Canberra, p. 118.
- Soler, P., 1987. Variations des teneurs en éléments mineurs (Cd, In, Ge, Ga, Ag, Bi, Se, Hg, Sn) des minerais de Pb-Zn de la province polymétallique des Andes du Pérou Central. *Miner. Deposita* 22, 135–143.
- Spikings, R., Reitsma, M., Boekhout, F., Miskovic, A., Ulianov, A., Chiaradia, M., Schaltegger, U., 2016. Characterisation of Triassic rifting in Peru and implications for the early disassembly of western Pangaea. *Gondwana Res.* 35, 124–143.
- Terrones, A., 1949. La estratigrafía del distrito minero de Morococha. *Sociedad Geológica del Perú* 2, 1–15.
- Titley, S.R., 1993. Characteristics of high-temperature, carbonate-hosted massive sulphide ores in the United States, Mexico and Peru. *Geol. Assoc. Can. Spec. Pap.* 40, 585–614.
- Todd, E.C., Sherman, D.M., Purton, J.A., 2003. Surface oxidation of chalcopyrite (CuFeS₂) under ambient atmospheric and aqueous (pH 2–10) conditions: Cu, Fe L and O K-edge X-ray spectroscopy. *Geochim. Cosmochim. Acta* 67, 2137–2146.
- Tolcin, A.C., 2015. Indium: USGS Mineral Commodity Summaries. <https://s3-us-west-2.amazonaws.com/prd-wret/assets/palladium/production/mineral-pubs/mcs/mc_s2015.pdf>.
- Torro, L., Melgarejo, J., Gemmrich, L., Mollinedo, D., Cazorla, M., Martínez, A., Pujol-Solá, N., Farré-de-Pablo, J., Camprubí, A., Artiaga, D., Torres, B., Alfonso, P., Arce, O., 2019a. Spatial and temporal controls on the distribution of indium in xenothermal vein deposits: The Huari Huari District, Potosí, Bolivia. *Minerals* 9, 304–340.
- Torro, L., Cazorla, M., Melgarejo, J., Camprubí, A., Gemmrich, L., Campeny, M., Artiaga, D., Torres, B., Martínez, A., Tarrés, M., Mollinedo, D., Alfonso, P., Arce, O., 2019b. Indium Mineralization in the Volcanic Dome-Hosted Animas-Chocaya-Siete Suyos Polymetallic Deposit, Potosí, Bolivia. *Minerals* 9, 604–642.
- Warren, H.V., Thompson, R.M., 1945. Sphalerites from western Canada. *Econ. Geol. Bull. Soc. Econ. Geol.* 40, 309–335.
- Wei, C., Huang, Z.L., Yan, Z.F., Hu, Y.S., Ye, L., 2018. Trace element contents in sphalerite from the Nayongzhi Zn–Pb Deposit, Northwestern Guizhou, China: insights into incorporation mechanisms, metallogenic temperature and ore genesis. *Minerals* 8, 490.
- Wilson, S.A., Ridley, W.I., Koenig, A.E., 2002. Development of sulfide calibration standards for the laser ablation inductively coupled plasma mass spectrometry technique. *J. Anal. Atom. Spectrom.* 17, 406–409.
- Wilson, J., 2019. Character and Genesis of Indium Mineralization, East, Kemptonville, Nova Scotia. M.Sc. thesis. University of Windsor, Ontario, Canada, p. 115.
- Winkler, C., 1886. Germanium, Ge, ein neues, nichtmetallisches Element. *Deutschen chemischen Gesellschaft* 19, 210–211.

Wood, S.A., Samson, I.M., 2006. The aqueous geochemistry of gallium, germanium, indium and scandium. *Ore Geol. Rev.* 28, 57–102.

Xu, J., Cook, N.J., Ciobanu, C.L., Li, X., Kontonikas-Charos, A., Gilbert, S., Lv, Y., 2020. Indium distribution in sphalerite from sulfide–oxide–silicate skarn assemblages: a case study of the Dulong Zn–Sn–In deposit, Southwest China. *Miner. Deposita*. <https://doi.org/10.1007/s00126-020-00972-y>.